MODELLING AND SIMULATION OF FRICTION IN METAL FORMING APPLICATIONS

A THESIS SUBMITTED TO
THE GRADUATE SCHOOL OF NATURAL AND APPLIED SCIENCES
OF
MIDDLE EAST TECHNICAL UNIVERSITY

BY

MURAT BAŞPINAR

IN PARTIAL FULFILLMENT OF THE REQUIREMENTS
FOR
THE DEGREE OF DOCTOR OF PHILOSOPHY
IN
MECHANICAL ENGINEERING

FEBRUARY 2024

Approval of the thesis:

MODELLING AND SIMULATION OF FRICTION IN METAL FORMING APPLICATIONS

submitted by **MURAT BAŞPINAR** in partial fulfillment of the requirements for the degree of **Doctor of Philosophy in Mechanical Engineering, Middle East Technical University** by,

Prof. Dr. Naci Emre Altun
Dean, Graduate School of **Natural and Applied Sciences**

Prof. Dr. Mehmet Ali Sahir Arıkan
Head of the Department, **Mechanical Engineering**

Prof. Dr. Haluk Darendeliler
Supervisor, **Mechanical Engineering, METU**

Examining Committee Members:

Prof. Dr. İlhan Konukseven
Mechanical Engineering, METU

Prof. Dr. Haluk Darendeliler
Mechanical Engineering, METU

Prof. Dr. Can Çoğun
Mechatronics Engineering, Çankaya University

Asst. Prof. Dr. Orkun Özşahin
Mechanical Engineering, METU

Asst. Prof. Dr. Şehram Dizeci
Mechanical Engineering, TED University

Date: 23.02.2024

I hereby declare that all information in this document has been obtained and presented in accordance with academic rules and ethical conduct. I also declare that, as required by these rules and conduct, I have fully cited and referenced all material and results that are not original to this work.

Name Last name : Murat Başpınar

Signature :

ABSTRACT

MODELLING AND SIMULATION OF FRICTION IN METAL FORMING APPLICATIONS

Başpınar, Murat
Doctor of Philosophy, Mechanical Engineering
Supervisor: Prof. Dr. Haluk Darendeliler

February 2024, 77 pages

In this study, a generalized friction model is proposed to be applied in metal forming processes. Friction model takes into account junction growth of asperities during combined loading and in order to represent real life cases. Asperities are defined by a curved surface such that elliptical contact is obtained between sheet and tooling. Curved surfaces with radius of curvature ratio of 0.5, 0.6, 0.8 and 1 are considered. Approximation equations are derived for junction growth until sliding inception for combined loading with sticking assumption. Lubrication mechanism is applied by solving the modified Reynolds equation. A finite element solution of rough contact zone is applied to solve lubricant pressure. Contact patch method is used to calculate the shear stress generated by rigid tooling asperities that penetrate into deformable asperities of workpiece. A fast and robust solid (real) contact area estimation approach is proposed to obtain relation between normal load and solid (real) contact area.

A cylindrical cup drawing process is selected to apply the proposed friction model and calculate coefficients of friction along a radial line. Real surface roughness of the undeformed steel blank material is measured by an optical 3D surface roughness measurement insturement for a sample area. Deep drawing process is performed up to 35 mm cup height then; strain and punch force measurements are taken and an iterative method is used during simulations at every 5 mm cup height. Surface simplification is applied on the real surface asperities and assumed to be repetative throughout the blank.

Keywords: Friction model, sliding inception, junction growth, curved surface contact, elliptical contact area, deep drawing process

ÖZ

METAL FORM VERME UYGULAMALARINDA SÜRTÜNMENİN MODELLENMESİ VE SİMÜLASYONU

Başpınar, Murat
Doktora, Makina Mühendisliği
Tez Yöneticisi: Prof. Dr. Haluk Darendeliler

Şubat 2024, 77 sayfa

Bu çalışmada; metal şekillendirme işlemlerinde uygulanmak üzere genelleştirilmiş bir sürtünme modeli önerilmiştir. Sürtünme modeli; birleşik yüklemede pürüzlerin temas alanı genişlemesini gerçek hayat uygulamalarına yansıtmak amacıyla hesaba katmaktadır. Pürüzler sac ve kalıplar arasında eliptik bir temas yüzeyi oluşacak şekilde, üç boyutlu bir yüzey ile tanımlanmıştır. Eğim yarıçapı oranları 0,5, 0,6, 0,8 ve 1 olan eğimli yüzeyler ele alınmıştır. Birleşik yük altında yapışma varsayımı ile kayma başlangıcına kadar temas alanı genişlemesi için yaklaşık denklemler türetilmiştir. Yağlama mekanizması değiştirilmiş Reynolds denklemi çözülerek uygulanmıştır. Yağ basıncını çözmek için sonlu elemanlar yöntemi pürüzlü temas alanına uygulanmıştır. Şekil değiştirebilen iş parçası pürüzlerine nüfuz eden iş kalıplara ait sert pürüzlerin yarattığı kesme gerilmesi temas parçası yöntemi kullanılarak hesaplanmıştır. Normal yük ve katı (gerçek) temas alanı arasında ilişkiyi saptamak için hızlı ve kararlı katı (gerçek) temas alanı hesaplayan bir yaklaşım önerilmiştir.

Ortaya konan sürtünme modelini uygulamak ve radyal bir çizgi boyunca sürtünme katsayılarını hesaplamak için bir silindirik kap çekme işlemi kullanılmıştır. Deforme olmamış çelik iş parçası malzemesinin gerçek yüzey pürüzlülüğü, örnek bir alan için üç boyutlu optik pürüzlülük ölçüm aletiyle ölçülmüştür. Derin çekme işlemi 35 mm çekme derinliğine kadar uygulanmış, birim uzama ve zımba kuvveti ölçümleri alınmıştır ve simülasyon sırasında her 5 mm kap derinliğinde bir yinelemeli metot kullanılmıştır. Yüzey sadeleştirme gerçek yüzey pürüzlerine uygulanmıştır ve taslak boyunca tekrarlayan yapıda olduğu varsayılmıştır.

Anahtar Kelimeler: Sürtünme modeli, kayma başlangıcı, temas alanı genişlemesi, eğimli yüzey teması, eliptik kontak alanı, derin çekme işlemi

To my family

ACKNOWLEDGMENTS

The author wishes to express his sincere gratitude to his supervisor dear departed Prof. Dr. Metin Akkök who offered invaluable support and criticism which formed the basis of this work. Author wishes to thank for the 15 years of endless encourage and guidance through the graduate studies.

The author is deeply grateful to Prof. Dr. Haluk Darendeliler whose support and expertise after taking over the supervision have enabled to be the PhD study to be completed within the specified time frame. Theoretical approaches of the study met up with real life with his guidance. Without his guidance and help, the level of maturity reached would not have been possible.

The author would also like to thank his family and colleagues for their patience and support throughout this work.

TABLE OF CONTENTS

CHAPTERS

APPENDICES

LIST OF TABLES

TABLES

LIST OF FIGURES

FIGURES

LIST OF SYMBOLS

SYMBOLS

A : Contact area

A_0 : Initial contact area

A_{sol} : Solid contact area

D : Distance between mean line of asperities and smooth tool surface

d_d : Distance between mean line of summits and smooth tool surface

E' : Equivalent modulus of elasticity

F_S : Shear force

F_{sol} : Shear force due to solid contact

h : Local lubricant film thickness

L_c : Critical normal load at full stick

l_x : Total mesh length in x direction

l_y : Total mesh length in y direction

n : Density of asperities

p_0 : Average pressure

P_c : Critical normal load at yield inception

P* : Non-dimensional normal load (P/L_C)

P : Normal load

Q : Tangential load

R_a : Arithmetic average of surface heights

R_q : Root mean square (RMS) roughness

R_x : Radius of curvature in x direction

R_y : Radius of curvature in y direction

V : Sliding velocity

β : Average radius of summits

η : Dynamic viscosity

σ_s : Standard deviation of summits

τ_{BL} : Lubricant boundary layer shear stress

τ_{lub} : Lubricant shear stress

τ_{sol} : Solid shear stress

τ_{total} : Total shear stress

Φ_P : Pressure flow factor

Φ_S : Shear flow factor

ν : Poisson’s ratio

CHAPTER 1

INTRODUCTION

1.1 Background and Motivation

Friction occurs at the interface surface of the contacting bodies under loading and in order to increase the efficiency of mechanical systems, accurate calculation of the coefficient of friction plays an important role. Friction calculation is mainly affected by the surface micro and macro roughnesses of contacting bodies and lubrication regime at the interface. Surface roughness has been mostly represented as asperities defined by spherical surfaces in literature due to its simplicity but, asperities defined by curved surfaces are more suitable for real life surfaces representation [1,2]. Asperities defined by curved surfaces have directional geometric properties with respect to the relative movement of the surfaces.

Friction and lubrication must be carefully controlled at contacting surfaces of metal forming processes since sufficient control of the deformed material. Thick lubricant decreases coefficient of friction, metal contact and may alter formability. In case of thin lubricant at interface, higher metal-to-metal contact ratio increases coefficient of friction with restricted material flow and may cause excessive thinning. Therefore, surface quality of the final products and surface flaws are highly affected by friction at interfaces and deeper tribological investigations are needed. The need for advanced friction models rise day by day in tribology area.

Metal forming processes include wide range of materials with light to excess loading conditions in their own nature. Studies focused on derivation of approximation equations for the change of contact area under normal loading and combined loading starting from elastic to plastic deformation range. Non-linear behaviour of elastic-plastic deformation makes it difficult to describe mathematically.

In this study, a more comprehensive and generalized friction model is introduced and the loading conditions are obtained from the numerical analysis of a cylindrical cup drawing of a steel sheet made of DKP6112. Asperities defined by curved surfaces are used to represent surface roughness. Junction growth is investigated for combined loaded bodies up to sliding inception point with full sticking assumption. Approximation equations are introduced for contact area change with additional tangential load. An interpolation data is created in order to calculate solid (real) contact area under normal load as a novel approach. Lubrication effects are introduced and calculated in a finite element approach of Shisode et al. [3].

1.2 Stribeck Curve and Lubrication Regimes

Almost at every contact interface lubricant exist whether at film form, starved or flooded condition. Existance of lubricant decreases the metal-to-metal contact and therefore; lower the coefficient of friction at interface and lower shear stresses. There are different lubrication regimes called boundary, mixed and hydrodynamic regimes which are defined by the amount of lubricant at the interface and relative velocity of the contacting bodies. A generalized Stribeck curve is shown in Figure 1.1, where coefficient of friction change is related to a non-dimensional parameter based on relative velocity, lubricant dynamic viscosity and normal load. Different lubrication regimes can also be observed from Stribeck curve trend changes, which are schematically represented in Figure 1.2.

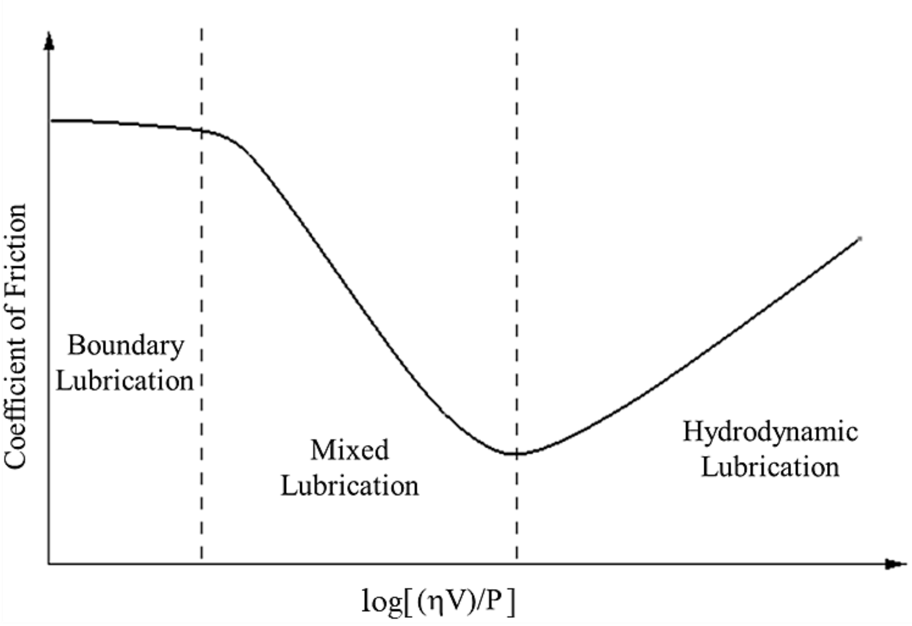

Figure 1.1. Generalized Stribeck Curve [4]

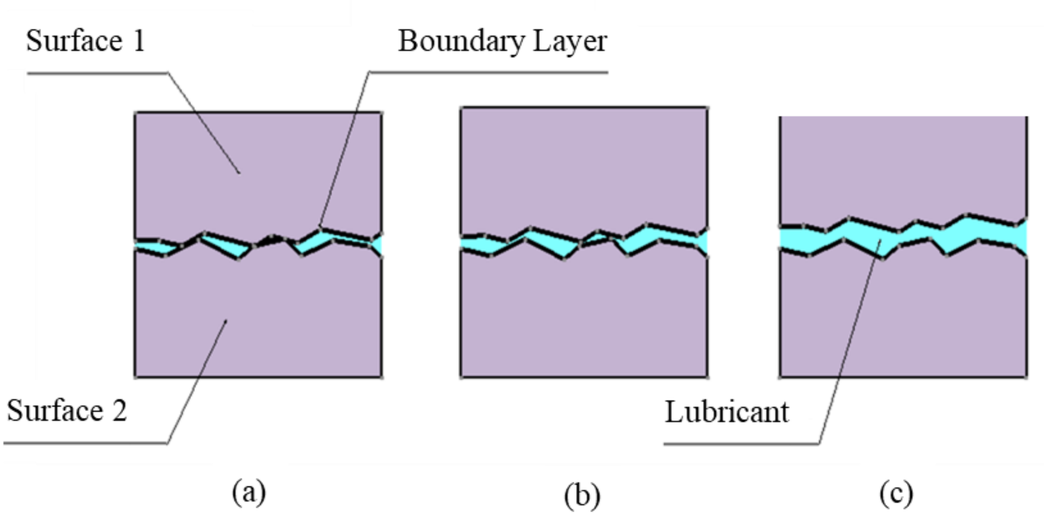

Figure 1.2. (a) Boundary, (b) mixed and (c) hydrodynamic lubrication representation [5]

1.2.1 Boundary Lubrication

Boundary lubrication is molecular mechansim of friction and schematic representation is shown in Figure 1.2. Boundary lubrication is the result of shearing of the covering boundary films (chemically reacted) generated at the outer surface of metallic materials. Thin monolayers are due to the absorption of the hydrocarbons, alcohol or fatty acids by the surface. There are three different mechanism of boundary film formation which are physical absorption, chemical absorption and chemical reaction. Schematic representation of different boundary layer formations are shown in Figure 1.3 [4].

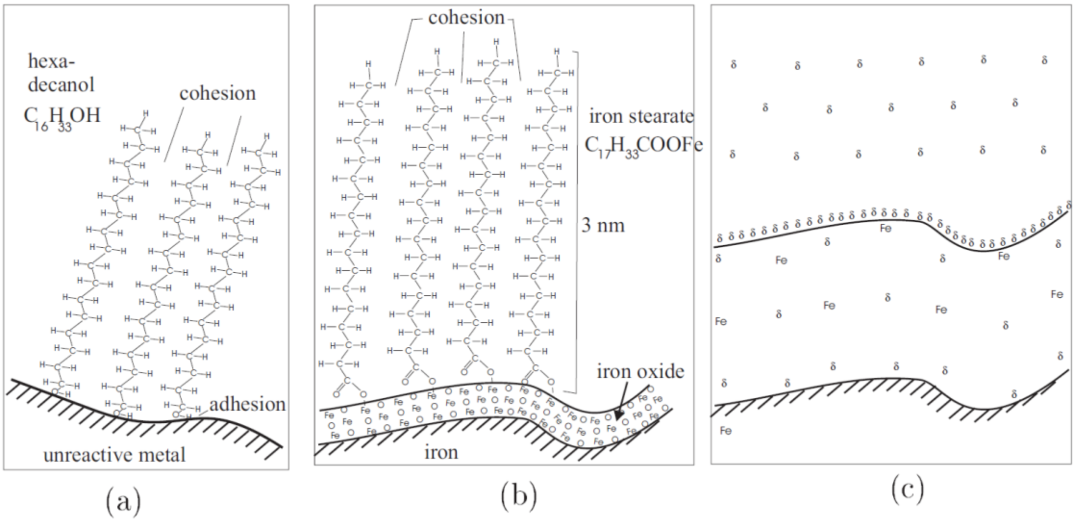

Figure 1.3. Boundary Layer Formations a) Physical absorption, b) chemical absorption and c) chemical reaction [4,6]

1.2.2 Mixed Lubrication

Mixed lubrication is the transition zone from boundary to hydrodynamic lubrication. Surfaces are partly separated and partly in contact. Load carried by lubricant increases while solid-to-solid contact decreases. If load is kept same; increasing the relative velocity decreases coefficient of friction and reaches the minima at the end of mixed lubrication regime. Schematic representation of mixed lubrication contact is shown in Figure 1.2.

1.2.3 Hydrodynamic Lubrication

In the hydrodynamic lubrication regime surfaces are highly separated. After the minimum in Stribeck curve, transition from mixed lubrication regime starts. While keeping the same normal contact load, increasing the relative velocity increases coefficient of friction in almost a linear trend. Mostly this type of lubrication is observed in bearings and pistons where flooded lubricant exists at contact interface. Schematic representation of hydrodynamic lubrication contact is shown in Figure 1.2.

1.3 Objective of This Research

This study aims to fill the gap between real life cases observed under high normal forces and more simpler assumptions in literature such as treating asperities as spherical surfaces [7,8]. Lubrication calculations of statistically defined surfaces are very rough estimates to be solved node by node. A more specific and local solution of asperities are needed in order to calculate correct coefficient of friction. This study proposes novel approaches for calculating solid (real) contact area and domain of approximation equations for junction growth are expanded to include curved surfaces with different radius of curvature ratios. Modified Reynolds equation is solved in order to include surface roughness effects.

1.4 Outline of the Thesis

In this section the outline of the thesis is summarized. In Chapter 1; background and motivation of the PhD study are described and importance of the coefficient of friction calculation is emphasized. Lubrication regimes and Stribeck curve are then introduced which is used in lubrication system classification. Purpose and objectives of the study is given at the end of the chapter.

In chapter 2; literature survey on junction growth and deep drawing characteristics are briefly described. Friction models and main approaches are categorized in four different categories.

In Chapter 3; Reynolds equation and flow factors are introduced which are used to solve pressure distribution of flow between two rough relatively moving surfaces. Roughness parameters are defined and equations are presented related to shear force calculation, lubrication solution and definition of surface roughness.

In Chapter 4; the proposed friction model, deep drawing simulation, real surface roughness and simplification, sliding inception and approximation equations, solid (real) contact area, lubrication model, asperity ploughing model, coefficient of friction calculation are presented. Steps to be followed during application of the proposed friction model is shown in a flow chart at the end of the chapter.

In Chapter 5; results of the deep drawing simulations are presented and discussed. In final chapter; conclusions about simulating the real processes with the proposed friction model are made. Reasons of errors in coefficient of friction calculation and further possible improvements are explained in detail.

CHAPTER 2

LITERATURE SURVEY

In experiments it was found that, the solid (real) contact area was smaller than the nominal contact area and it increased due to application of tangential load until the maximum static friction is reached [9-13]. Then, increasing the tangential load resulted in sliding at the interface. Early studies by Cattaneo [14] and Mindlin [15] focused on elastic contact of contacting spherical bodies under combined loading and investigated the contact area in two different regions; a sticking region at the center and surrounded by a slip annulus which is the result of additional tangential loading. This annular region extends to center until sticking region diminishes when sliding starts. Another experimental study by McFarlane and Tabor [16] related the contact area to adhesion force indirectly; which was based on contact of a soft and a hard body. A steel ball loaded against a soft indium flat resulted in contact area increase up to 14 times of the initial contact area at room temperature.

More recent studies aim to differentiate the presliding regime by using tangential stiffness and later studies focused on determination of sliding inception with sticking contact assumption. Etsion et. al [17] investigated the presliding regime and used non-dimensional parameters to formulate static friction evolution and tangential stiffness at the interface. A spherical body which is in contact against a rigid flat surface is loaded under combined loading with sticking assumption. In order not the exceed presliding regime, tangential displacement is limited to the normal deflection of the spherical body under initial pure normal loading. In study of Etsion et. al [18], Coulomb static friction approach was used to solve sliding inception of an elastic perfectly plastic spherical body under combined loading. Maximum tangential load that can be supported by interface was calculated at sliding inception. Approximation equations were derived for static coefficient of friction by using FEM solutions.

Etsion et. al [19] solved spherical body contact against a rigid flat under different contact assumption which are full stick and perfectly-slip contact conditions. Study investigated the effects of wide range of mechanical properties of the deformable body on the critical interference and critical load. Mathematical and FEM solutions were obtained for ductile and brittle materials. Von Mises stress and maximum tensile stress were used to define the start of failure for ductile and brittle materials respectively. Etsion et. al [20] investigated the junction growth until sliding inception, which is the loss of contact stability. Deformation mechanisms of a combined loaded spherical body were explained separately. FEM results were compared with study of Tabor. Study claimed that the junction growth was dependent on the initial normal preload.

Finite element solutions and mathematical models were examined by experimental approach of Etsion et. al [21]. Junction growth of an elastic-plastic body under combined loading was measured in real time by using optical devices. Study proposes that up to 45% of initial contact area (under only normal preload) enlarged after additional tangential loading. Study claimed that results were well correlate with medium and high preloads.

Junction growth of combined loaded bodies, defined by spherical surfaces, against rigid flat and its deformation mechanisms were well understood but, simulations showed that as deformable body geometry deviated from radius of curvature ratio of 1, different junction growth trends and sliding inception curves were observed in results of finite element simulations. Similarly; the ratio of maximum tangential load (Q_{max}), that can be supported by the interface, to normal load (P) varies up to 30% which must be taken into account. Also; a new criterion is proposed for easier determination of sliding inception point. In order to eliminate scaling factors, simulations are performed for curved bodies with highest radius of curvature of 10 μm. The aim of this study is to obtain non-dimensional approximation equations to be used in coefficient of friction calculations where junction growth under combined loading is significant and applicable to a wider range of geometries.

Başpınar and Akkök [22] investigated deep drawing of steel sheet in detail where coefficient of friction is calculated for every contact pair by using two different friction models. One of them is solid contact based approach of Khonsari [23] and another is hydrodynamic approach of Wilson [24]. A transition h/σ value is proposed to differentiate which model needs to be used. It is proposed that the punch nose is not effective in deformation of blank while punch radius and friction at this interface is the major deformation region. Coefficient of friction at punch radius region is calculated between 0.05-0.1 which shows that using a constant value is a rough estimation. Another important region is the die radius where continuous deformation of the flowing blank material under blank holder starts to deform.

2.1 Friction Models in Literature

In literature, there are many friction model approaches based on different assumptions. According to Westeneng [4], four different main assumptions exist which are stochastic contact models, numerical contact models, contact models based on bulk deformation and contact models based on volume conservation. All the models assume a rigid smooth tooling surfaces deforming soft asperities on rough workpiece. Elastic, combination of elastic and plastic or totally plastic deformation of asperities are considered and mathematically described in three different topics.

2.1.1 Stochastic Contact Models

Stochastic contact models assume that surface roughnesses are represented as spherical summits that are distributed around the mean plane of summits. All spherical summits have the same radius β. $\phi_s(s)$ is the statistical height distribution and σ_s is the standard deviation of the surface height. Distance between mean plane of asperities and smooth surface is called d while distance between mean plane of summits and smooth surface is called d_d.

Nominal pressure is calculated by the normal load at the interface divided by the nominal contact area. Since surfaces are not perfectly smooth, solid (real) contact area is smaller than the projected area. Additionally, not all the summits establish metal-to-metal contact. Number of contacting nodes increases until the contact load is balanced by deformed summits. Stochastic models calculate solid (real) contact area in multiple ways which can be summarized below.

Greenwood and Williamson [7] described in their model that, all asperities have the same end radius with a hemispherical shape called as summits and deform only elastically. All asperities are treated separately therefore; asperity position, cumulation or interaction is omitted.

Greenwood and Tripp [8] extended the study of Greenwood and Williamson to asperities with tips shaped as paraboloidal shapes. As a similar approach, all asperities have the same geometry and position or interactions are omitted.

Onions and Archard [25] also improved and extended the study of Greenwood and Williamson with an additional parameter which is the exponential correlation function β'. N is the ratio of peaks to ordinates and C is the non-dimensional asperity curvature. $f'(s, C)$ is the probability density of summits.

An elastic-plastic deformed asperity summit model is proposed by Chang et al. [26] with the assumption of volume conservation during plastic deformation.

Elastic and perfectly plastic deformed asperity summits are derived in two different sets of equation by Halling et al. [27] The following equations are used to calculate nominal pressure and contact area separately. Plasticity index is denoted by ψ.

2.1.2 Numerical Contact Models

Contact models that describe the surface asperities mathematically, treat the asperities as square bars. Pressure on individual bars is related to the displacement of the bar and assumed only to be deformed elastically. Application of this type contact models are limited since elastic deformation does not dominate metal forming applications. Numerical contact models are proposed by Liu et al. [28] and Webster and Sayles [29] in literature.

2.1.3 Contact Models Based on Bulk Deformation

In metal forming applications, bulk deformation effects are important for the roughening and flattening of a surface. Studies are based on wedge shaped asperities as shown in Figure 2.2. Two different mechanisms are followed which are smooth workpiece asperities are roughened and workpiece asperities are smoothing. Well known models in literature are proposed by Sutcliffe [30], Wilson and Sheu [31] and Kimura and Childs [32].

2.1.4 Contact Models Based on Volume Conservation

A volume conservation based contact model is developed by Pullen and Williamson [33]. The study originated from experiments that solid (real) contact area is not proportional to the nominal pressure. The volume of uniform rise in the valleys is equal to the sum of the total volume of indented asperities. This model does not take into account work hardening and bulk deformation effects. Uniform rise in the valleys is calculated from the following equations for an any arbitrary shaped asperity.

CHAPTER 3

LUBRICATION AND ROUGHNESS

In this chapter, basics and terminology of lubrication and surface roughness are defined and related equations are proposed. General Reynolds equation is modified with shear and pressure flow factors in order to include surface roughness effects to the solution with nodal differentiation method. Roughness parameters such as arithmetic average roughness, root mean square roughness, skewness, kurtosis and Gaussian distribution are explained in detail.

3.1 Reynolds Equation and Flow Factors

The modified Reynolds equation is used to calculate the lubricant pressure under high loading [3]. The modified Reynolds equation including surface effects is given below.

$$\nabla.(\frac{h_{avg}^3}{12\eta}\frac{\partial \boldsymbol{\Phi}_P}{\partial x}.\nabla\bar{P}) = \nabla.\left(\frac{h_{avg}(\boldsymbol{u}_1+\boldsymbol{u}_2)}{2} + \frac{\partial \boldsymbol{\Phi}_s}{\partial x}.\frac{R_q(\boldsymbol{u}_1+\boldsymbol{u}_2)}{2}\right) + \frac{\partial h_{avg}}{\partial t} \qquad (3.1)$$

where; $\boldsymbol{\Phi}_P$ and $\boldsymbol{\Phi}_S$ are the flow factors calculated due to surface irregularities and they are represented in matrix form.

$$\boldsymbol{\Phi}_P = \begin{bmatrix} \Phi_{Pxx} & \Phi_{Pxy} \\ \Phi_{Pyx} & \Phi_{Pyy} \end{bmatrix}, \boldsymbol{\Phi}_S = \begin{bmatrix} \Phi_{Sxx} & \Phi_{Sxy} \\ \Phi_{Syx} & \Phi_{Syy} \end{bmatrix}$$

$$\nabla = (\frac{\partial}{\partial x}, \frac{\partial}{\partial y})$$

R_q is the root mean square (RMS) of the combined roughness. In this case; R_q is the roughness of the sheet metal to be formed since tool roughness is negligible with respect to blank roughness. $\bar{P}(x, y)$ is the average local fluid pressure. $\boldsymbol{u}_1 = \boldsymbol{u}_1(x, y)$ is the velocity in x and y directions of surface 1 and $\boldsymbol{u}_2 = \boldsymbol{u}_2(x, y)$ is the velocity in x and y directions of surface 2.

Pressure flow factor for isotropic surface roughness Φ_{Pxx} is equal to Φ_{Pyy} and $\Phi_{Pxy} = \Phi_{Pyx} = 0$. Similar matrix properties and assumptions are used for the shear flow factor, $\boldsymbol{\Phi}_S$. For simplicity, flow is calculated in x direction only with no-flow assumption in y direction boundaries due to symmetry of forming process. Then;

$$\Phi_{Pxx} = \frac{Q_{rough}}{Q_{smooth}} \tag{3.2}$$

Q_{rough} and Q_{smooth} are calculated from following equations per unit width with pressure distribution $(P_B - P_A)/l_x$. Q_{rough} is calculated by averaging the flow between two surfaces with calculated pressure distribution.

$$Q_{smooth} = \frac{h_{avg}^3}{12\eta}\left(\frac{P_B - P_A}{l_x}\right) \tag{3.3}$$

$$Q_{rough} = \frac{1}{0.8^2 l_x l_y}\int_{0.1l_x}^{0.9l_x}\int_{0.1l_y}^{0.9l_y}\frac{-h^3(x,y)}{12\eta}\frac{\partial P}{\partial x}\partial x \partial y \tag{3.4}$$

In pressure flow factor calculation, relative movement of the surfaces are assumed to be stationary while $\partial P/\partial y = 0$ at side walls. Schematic representation of pressure flow factor calculation B.C.'s is shown in Figure 3.1.

Shear flow factor is due to relative movement of the contacting surfaces without effect of any pressure gradient. The effect of lubricant, which is entrapped at the rough surface valleys and transported due to movement, is calculated. The relation between velocities is assumed as $\mathbf{u}_1 = -\mathbf{u}_2 = \mathrm{U}_s/2$. Schematic representation of pressure flow factor calculation B.C.'s is shown in Figure 3.2. Then; matrix element Φ_{Sxx} is calculated by using the following equation;

$$\Phi_{Sxx} = Q_{rough}\left(\frac{2}{R_q U_s}\right) \tag{3.5}$$

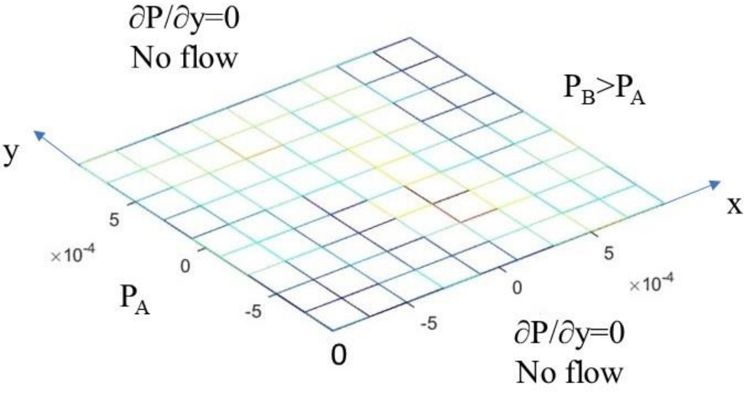

Figure 3.1. Schematic representation of pressure flow factor boundary conditions

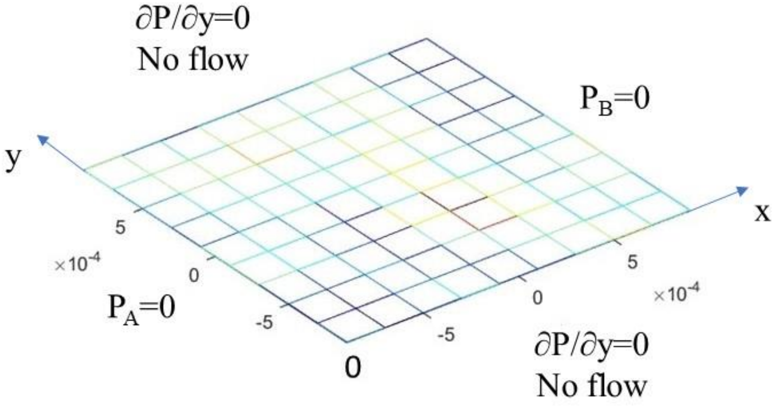

Figure 3.2. Schematic representation of shear flow factor boundary conditions

3.2 Surface Roughness Parameters

Surfaces of parts which are manufactured with different methods in the desired form and shape, in reality deviate from nominal. There are deviations in milimeter level and also micrometer level, if measured by surface profile measurement tools. Surface roughness can be described as micro (<10 μm) and macro roughness (>10 μm) according to measurement level. In this study, macro asperities are classified with radius of curvature larger than 10 μm in major direction. Change of roughness level is described in Figure 3.3 schematically. In another words surface roughness is limited by the resolution of the measurement tool and the degree of information needed by the user to define surface. There are hundreds of surface roughness parameters but, only a few of them are mostly used by literature. Commonly used surface parameters are R_a, R_q, skewness and kurtosis. Surface roughness measurements are taken for a sampling length and not throughout the whole surface.

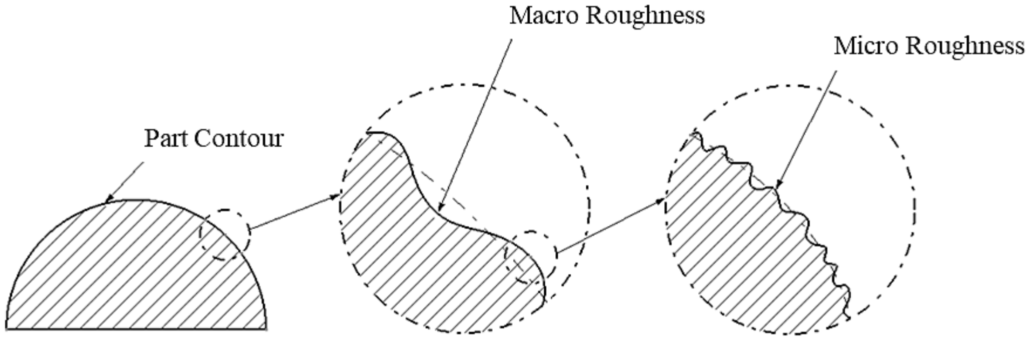

Figure 3.3. Surface roughness levels

Arithmetic average roughness is calculated by the following equations and each height is measured with respect to the mean line. Number of measurements are defined by the resolution of the measurement tool and sampling length. Summation of height values are divided by the number of heights. As a common approach mean line, y_m, is offset in order to coincide with $y = 0$ axis. R_a is used to represent arithmetic average roughness height.

$$R_a = \frac{1}{L}\int_0^L |y(x) - y_m|\, dx \tag{3.6}$$

and y_m is calculated from;

$$y_m = \frac{1}{L}\int_0^L y(x)dx$$

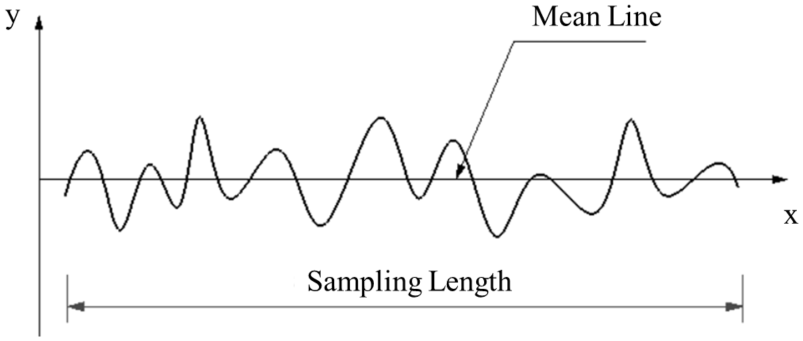

Figure 3.4 Surface roughness and mean line [5]

Root mean square (RMS) roughness is a similar definition to R_a but, calculation with the following equations gives close but different results. Mostly used in lubrication equations, definition of rough surface separation and lubricant film thickness. It is the root of surface height squares divided by sampling length. R_q is used to represent root mean square roughness.

$$R_q = \sqrt{\frac{1}{L}\int_0^L y(x)^2 dx} \tag{3.7}$$

Symmetric or normal distribution of surface heights is called as the Gaussian distribution and used in this study for simplification. Probability function (p) of Gaussian distribution and the curve is shown in Figure 3.5. Any other surface having different distribution than Gaussian is called a non-Gaussian surface.

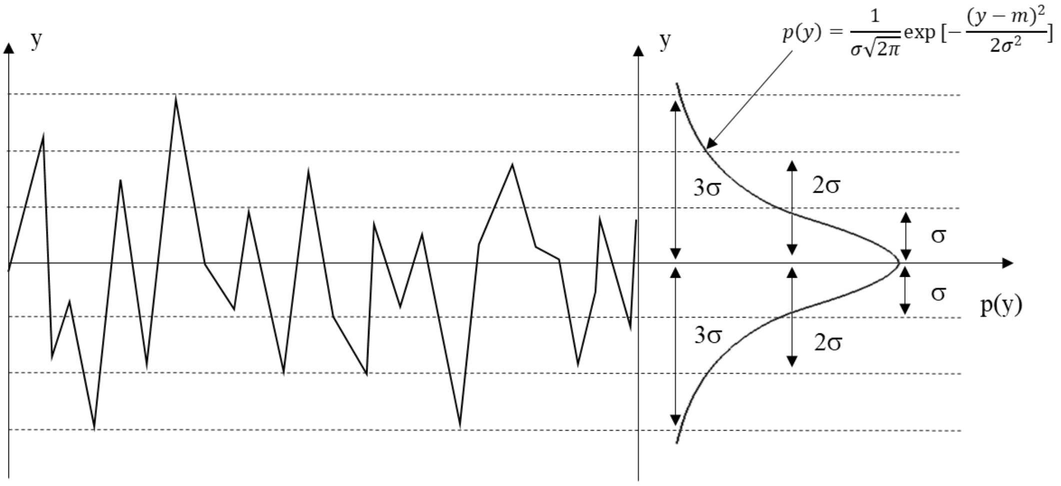

Figure 3.5 Gaussian distribution and function [34]

Skewness is simply the deviation of probability function either surfaces heights are accumulated above or below mean line. Skewness is 0 for a Gaussian surface and negative values indicate surface height density is higher above the mean line and vice versa. R_s value is used in the equation of skewness which is;

$$R_s = \frac{1}{R_q^3 L} \int_{-\infty}^{+\infty} y^3 p(y)\, dy \qquad (3.8)$$

Another related parameter is kurtosis and it is defined as the sharpness of the peaks of the surface. It is the fourth power of the skewness equation. Kurtosis is 3 for a Gaussian surface and higher values than 3 means needle-like sharp asperities. Kurtosis values smaller than 3 means more flattened asperities which is a good feature for a contacting surface.

$$R_k = \frac{1}{R_q^4 L}\int_{-\infty}^{+\infty} y^4 p(y)\, dy \tag{3.9}$$

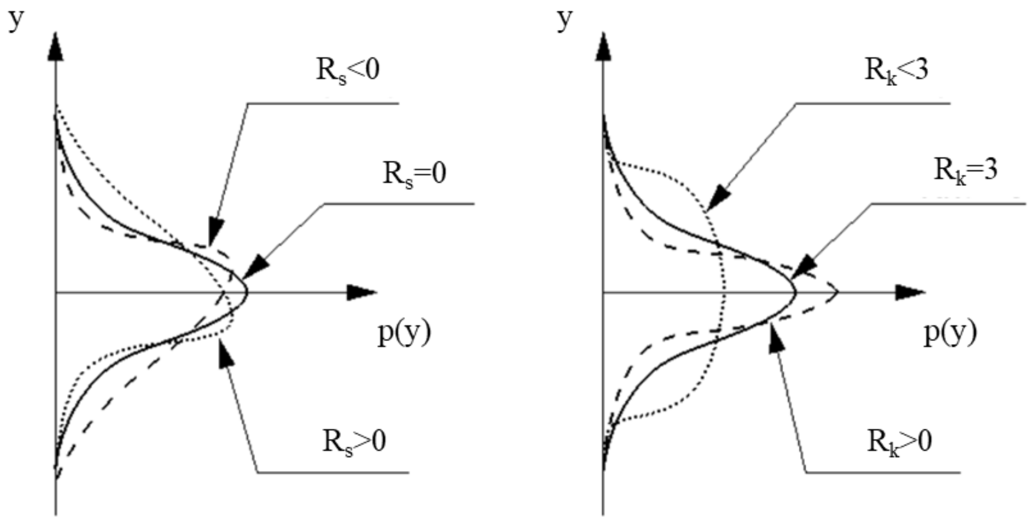

Figure 3.6 Skewness and kurtosis distributions for Gaussian and non-Gaussian surfaces [35]

CHAPTER 4

PROPOSED FRICTION MODEL AND DEEP DRAWING PROCESS

In this chapter, deep drawing process parameters are explained and important aspects of the process to be focused in later chapters are described in detail. Proposed friction model is explained in eight sub-chapters starting from deep drawing simulation, real surface roughness and simplification, curved surface contact, sliding inception and junction growth, solid (real) contact area, lubrication model, single asperity ploughing model and finally the calculation of the coefficient of friction.

4.1 Deep Drawing Process

Among the metal forming operations, deep drawing process is selected to be further investigated in this study. Since deformation of blank and its formability is highly affected by friction at the tooling and blank interfaces, there are different investigations of deep drawing process which focus on calculation of coefficient of friction at contact regions that occur during process. Die and blank holder is kept stationary while movement of the punch into the blank creates the final geometry of the cylindrical cup. During this plastic deformation of blank, coefficient of friction changes by time and different for each interface. A constant coefficient of friction can’t be assigned to an interface and must be updated throughout the process. Simulation and FEM models are described in following chapters.

As proposed by Başpınar and Akkök [22], friction calculations are focused on the punch radius and die radius regions. Other zones have very little effect on the formability or have no contact for coefficient of friction evaluation. Punch nose region barely contacts with the blank and blank holder avoid creation of wrinkles.

4.2 Proposed Friction Model and Sub-Components

The friction model proposed in this thesis consist of eight sub-parts; starting from simulation of sheet metal forming to calculation of coefficient of friction at every contacting points. Deep drawing process of a cylindrical cup is investigated due to advantage of axisymmetry. Every 0.64 x 0.64 mm contact piece along a radial line of the steel blank (DKP6112) is investigated separately. 0.64 mm dimensional limitation originates from the capability of the measurement device and repetative surface characterictics of the blank material due to manufacturing method. Each contact piece is assumed to have same rouhgness distribution and established of 456 x 456 nodes which equals 207936 nodes in total. It is seen that the surface asperities are oriented in the same direction. In later chapters, surface roughness is simplified by curved surfaces with different radius of curvatures. This method allows to treat asperities in macro level and calculate load carried by each macro asperity separately. Therefore; junction groth approximation equations can be applied to calculate enlarged real contact area.

Total load at a contact piece is the sum of solid-to-solid contact and load carried by the lubricant. Summation of the shear force generated by solid contact and lubricant flow between surfaces are divided by normal load to calculate coefficient of friction.

4.2.1 Deep Drawing Simulation

Deep drawing is performed for a blank made of steel sheet (DKP6112) with diameter of 100 mm and thickness of 1 mm. Material properties of DKP6112 are taken from study of Dizeci as shown in Table 4.1 [36]. In order to simplify and run simulation, constant coefficient of friction is set at all interfaces separately. There is a 1.5 mm clearance between die opening and punch in order not to deform blank excessively.

Table 4.1 Material properties of DKP6112 obtained by uniaxial tension tests [36]

UTT direction	0°	45°	90°
$E\ (GPa)$	141	139.9	150.5
ν	0.32	0.315	0.31
$\sigma_y\ (MPa)$	250	256	242
$K\ (MPa)$	643	668	632
n	0.247	0.252	0.241
r	1.34	0.99	1.67

A successful cylindrical deep drawing simulation is performed up to 35 mm height after 7 stages of friction calculation. Punch speed is set as 20 mm/s which is reached in 1.75 seconds. A constant blank holder force of 50 kN is set at maximum cup height which allows material flow while restricting wrinkle formation at flange region. FEM model of blank is meshed in 3D with 21293 tetrahedron shaped elements and 52665 nodes. Punch and die radius regions are fine meshed while smooth surfaces like punch nose are coarse meshed. In order to save simulation time, only half of the bodies are meshed and symmetry condition is used. Also; symmetry plane gives smooth distribution of nodes at same line with changing distance from center. Boundary conditions of the highlighted surfaces of die, blank holder and punch are shown in Figure 4.1, respectively.

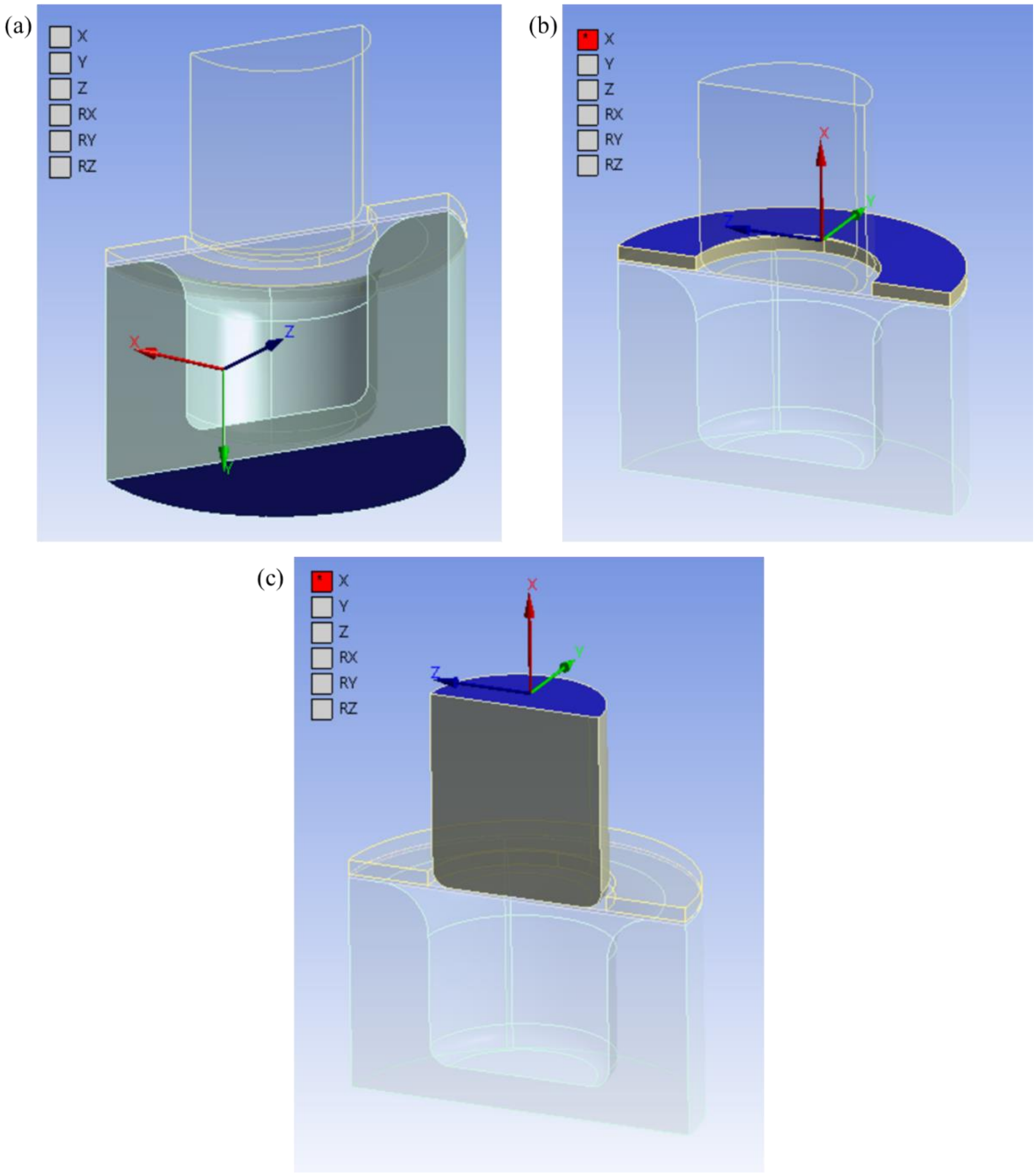

Figure 4.1 Boundary conditions of (a) die, (b) blank holder and (c) punch (red color indicates free movement or rotation)

Initial assumption of coefficient of friction for all interfaces is 0.26. Coefficient of friction is set to new average value and simulation re-run with new values. Previous coefficient of friction results are averaged at every simulation step. Results of thickness distribution, equivalent von Mises stress, pressure distribution and nodal coefficient of friction distribution are shown in Chapter 5. At the maximum punch height, contact of blank with the blank holder almost ends.

In order to optimize mesh and decrease simulation time, it is aimed to use the maximum element size as possible. Maximum element size is selected to be 1.28 mm and same results are obtained for smaller element sizes for comparison and verification purposes. Mesh quality is also verified by skewness and orthogonality values in FEM statistics. Skewness is the deviation of a deformed cell from a perfect shape cell. Orthogonality is the angular measurement of cell edges and cell faces. It is claimed by the FEM program that as the orthogonal quality mesh metrics spectrum reaches 1 (range between 0-1), mesh quality is excellent. On the contrary; as the skewness mesh metrics spectrum reaches 0 (range between 0-1), mesh quality is excellent. Skewness value is 0.2 and orthogonality value is 0.9 in simulations, which proves a high-quality mesh. It is proposed that skewness is a more effective metric for mesh quality of tetrahedron shaped elements.

4.2.2 Real Surface Roughness and Simplification

Surface characteristics of sheet metal parts are mainly affected by the manufacturing method used. Rolling process is mostly used where the compacting forces are determined by the material properties and sheet metal thickness. Similar surface defects with similar orientation are observed which repeat throughout the part. It is an efficient way to generalize the measured surface roughness while using in tribological calculations.

In order to represent real contact conditions of cylindrical cup drawing in the study, surface roughness of the steel blank (DKP6112) is measured by an optical 3D surface roughness measurement instrument, Alicona Infinite Focus. 456 x 456 points are measured with a resolution of 1.4 μm. Total of 0.64 x 0.64 mm area is digitized and shown in Figure 4.2.

Irregular measured surface roughnesses need to be converted into macro asperities defined by curved surfaces in order to apply friction model separately. 56 macro elliptical asperities are fitted into measured surface. Circle fitting method is applied to calculate radius of curvature in two perpendicular directions. Sample fitted elliptical asperities are shown in Figure 4.3. It is seen that the major radius of curvatures of macro asperities are oriented in the same direction.

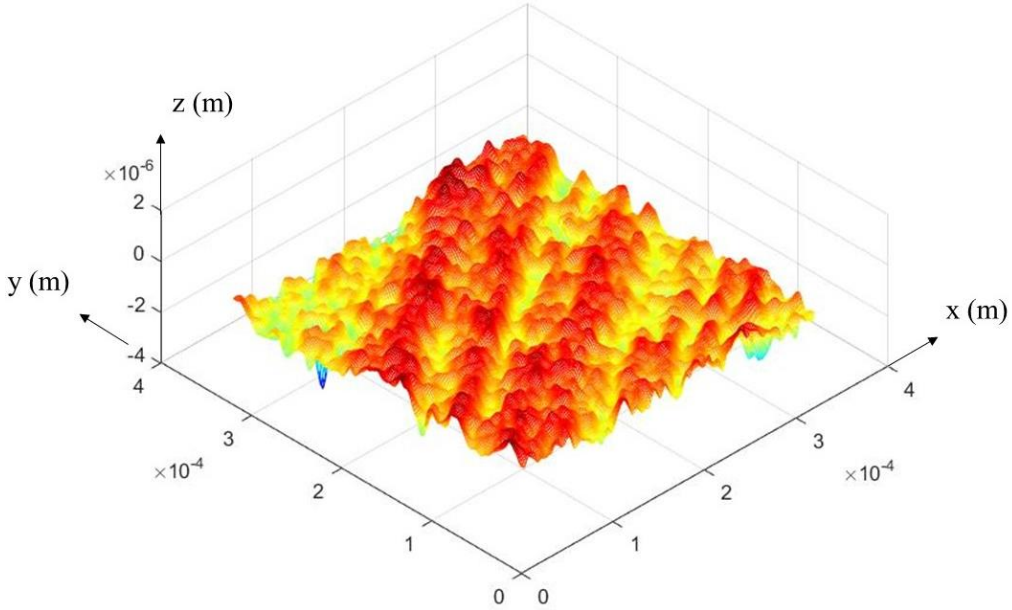

Figure 4.2 Schematic view of measured rough surface (quarter shown)

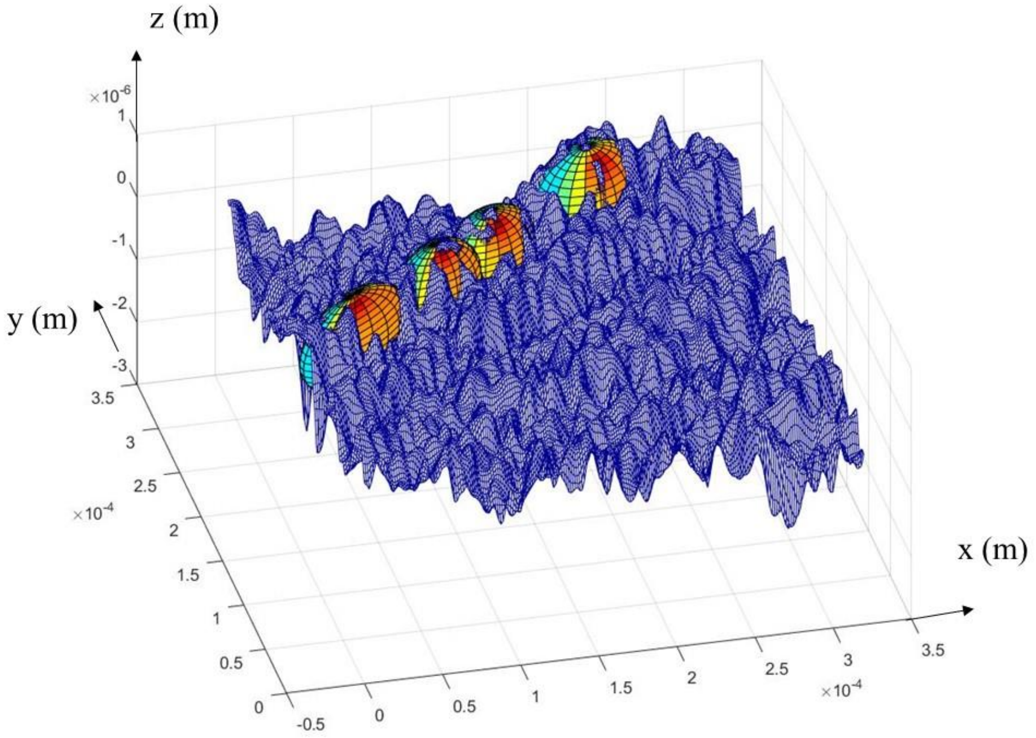

Figure 4.3 Schematic view of curved surfaces fitting to measured rough surface (quarter shown)

4.2.3 Curved Surface Contact

Surface roughness is investigated in two levels. Micro-level is more suitable for representing tooling surface roughness which is relatively small compared to blank roughness. Macro-level roughness approach is helpful to treat large surface geometries as simplified geometrical shapes. Most of the literature assume asperities defined by spherical surfaces for easier formulation and deal with a smaller number of parameters [37]. In this study, simulations and approximations are investigated for asperities defined by curved surfaces to be employed in macro-level approach. In order to account for realistic range of surface irregularities, curved surfaces are used instead of spherical surfaces.

4.2.4 Sliding Inception and Approximation Equations

As explained earlier, sliding inception is the point of deformation where no more tangential load can be supported at a normally loaded contact interface. The deformation mechanism under combined loading is that, with sticking assumption initial contact area does not move relatively, while contact area enlarges in the direction of the tangential load. Normal and tangential loads are applied to smooth rigid body as shown in Figure 4.4. This additional contact area is due to rising initial non-contacting surface of the deformable body. Contact area change is observed in Figure 4.5 for a spherical body under 10 times the critical load, P^*. 0%, 50% and 100% of the maximum tangential load that can be applied is shown separately.

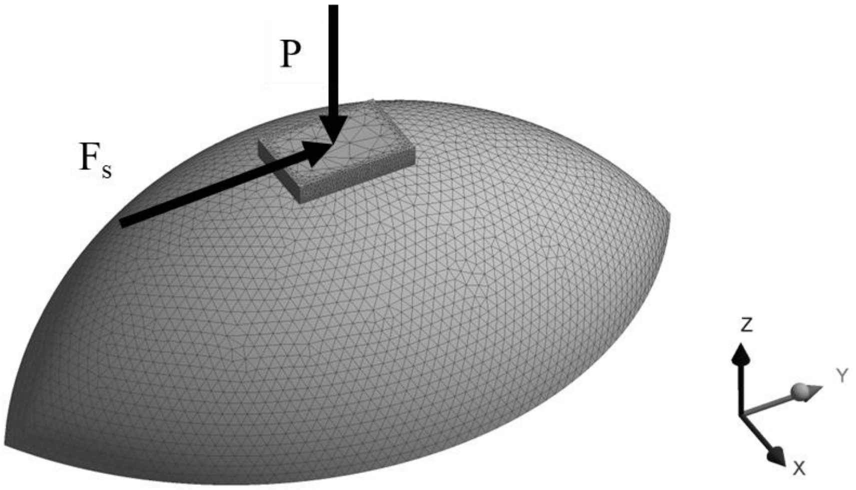

Figure 4.4 Normal and tangential loads applied on rigid flat body

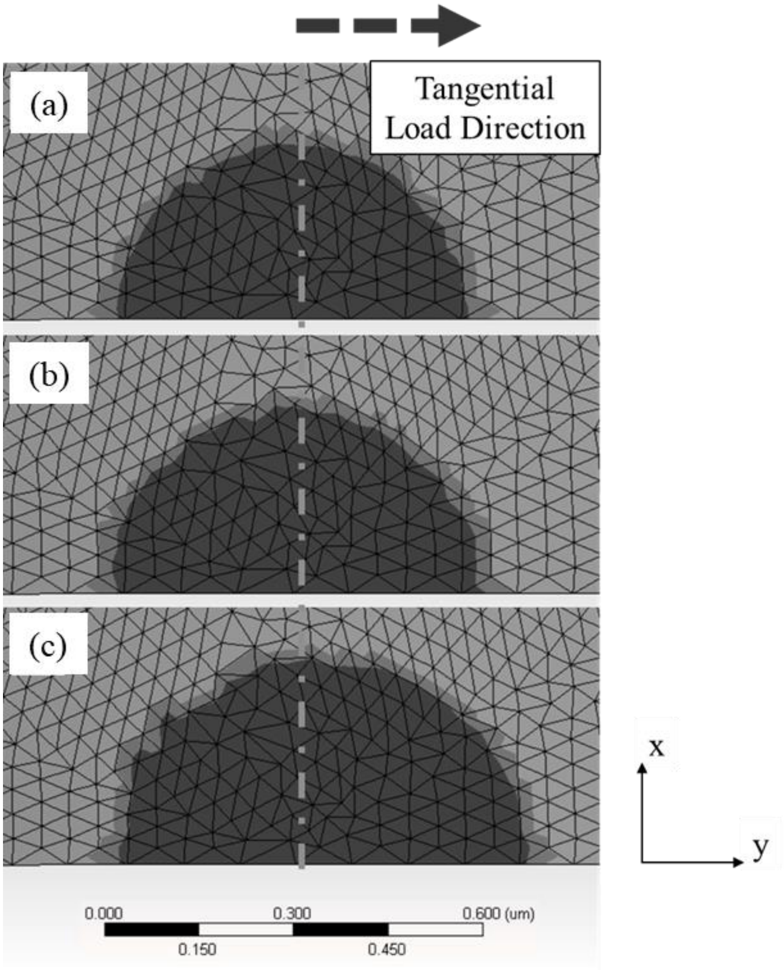

Figure 4.5 Contact area change with additional tangential loading at (a) 0%, (b) 50% and (c) 100% of the maximum tangential load ($P^* = 10$)

Junction growth occurs as the tangential load increases. There are abrupt changes after this point and there are different approaches and definitions to differentiate. Tangential stiffness is used as a parameter and also von Mises stress criterion for plastic yield is used. In this study, sliding inception is defined by the change of trend in total directional movement of rigid flat body.

4.2.4.1 Curved Surface Configurations for Approximation Equations

A set of bodies with different radius of curvatures are deformed in order to create an interpolation data. Radius of curvature ratios are varied from 0.4 to 1 and radius of curvature is set as 10 μm in principal direction. The reason is that, as the surface irregularities are in micrometer level, simulating bodies in the order of milimeters may cause scaling problems while relating normal load to deformation. Bodies are loaded in combination of normal load followed by a gradually increasing tangential load which is denoted as combined loading. Maximum tangential load changes with P^* value and almost equal to the maximum normal load at smaller P^* values down to 1.

Deformable body material is chosen to be structural steel with a yield strength of 250 MPa, modulus of elasticity of 200 GPa and Poisson's ratio of 0.3. Combined loaded flat body against deformable body is selected to behave rigid and do not deform or rotate. Only half of the body is modeled due to symmetry. Lower surface of the half body is fixed in space and restricted to move normal to symmetry plane as boundary condition. Another boundary condition is to restrict movement of rigid body only in symmetry plane without rotation. Rough contact is selected for interface which means relative movement of the contacting nodes are restricted.

A variable mesh sizing approach is used during meshing of the bodies. Deformation of the half body is effective within a very small area but; stress distribution effects a larger percentage of body. Also; a large number of nodes at the contact area is required to interpret contact area change over time. Four different zones are determined to gradually decrease mesh size which is highest at the vicinity of contact zone. And in order to eliminate abrupt mesh transition, 2 lighter mesh zones are employed before rough outermost mesh. All the contact effects due to combined loading within the half body, almost diminishes at the rough mesh zone which decreases simulation time and do not change results significantly. Maximum element size of meshes are 0.04 μm, 0.1 μm, 0.2 μm and 0.5 μm from finest to coarse respectively and FEM model is shown in Figure 4.6.

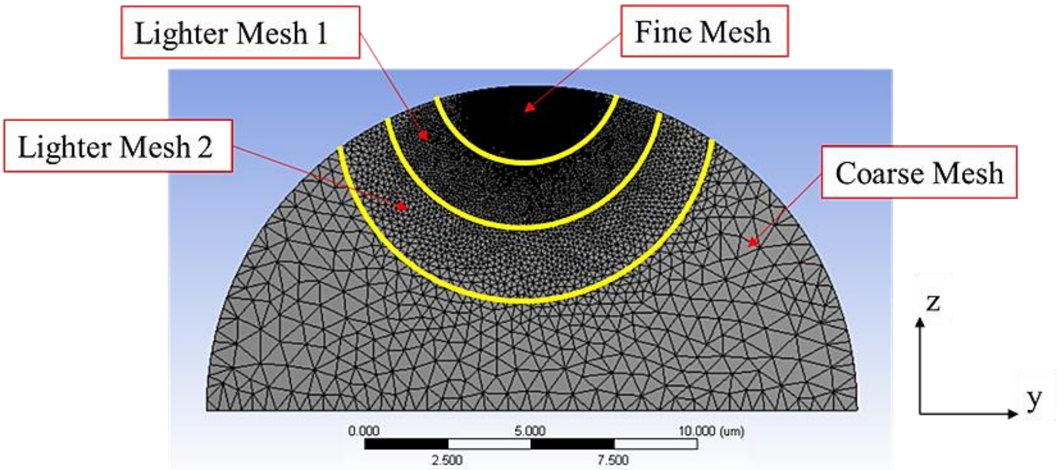

Figure 4.6 FEM of elliptical half body

4.2.4.2 Interpolation Data for Approximation Equations

In order to create an interpolation data for the deformation of bodies with different radius of curvatures against a rigid flat under combined loading, load range needs to be determined starting from critical load ($P^* = 1$). In study of Etsion et al. [38], critical load for ductile and brittle materials are calculated separately both for perfect slip and full stick conditions. P^* is a non-dimensional parameter which is calculated by dividing the normal load with critical normal load in full stick which is L_c. In literature, P^* values are investigated up to 500, which also corresponds to other studies which define it is the start of fully plastic deformation. Results from literature shows that as the P^* increases, tangential load percentage required for sliding inception decreases. L_c can be calculated from the following equations below. Since formulations are based on asperities defined by spherical surfaces, loads for bodies defined by curved surfaces are calculated for an equivalent spherical surface. Equivalent radius is calculated from the following formula;

$$\frac{2}{R_{eq}} = \left(\frac{1}{R_x} + \frac{1}{R_y}\right) \tag{4.1}$$

Critical load at yield inception of a normal loaded asperity defined by spherical surface is calculated from;

$$P_c = \frac{\pi^3}{6} C_\nu^3 Y \left(R(1-\nu^2)\frac{Y}{E}\right)^2 \tag{4.2}$$

where C_ν is a function of Poisson's ratio;

$C_\nu = 1.234 + 1.256\nu$

Then, the critical load at full stick is calculated from the following relation;

$$L_c = P_c\big(8.88\nu - 10.13(\nu^2 + 0.089)\big) \tag{4.3}$$

Loads for each bodies with different radius of curvatures and P^* values are listed in Table 4.2. P^* values are determined as 5, 10, 50, 100, 250 and 500.

Table 4.2 Load range for bodies with different radius of curvature configurations for $R_y = 10\ \mu m$

Radius of Curvature Ratio (R_x/R_y)	$P^* = 5$	$P^* = 10$	$P^* = 50$	$P^* = 100$	$P^* = 250$	$P^* = 500$
1	3.75 μN	7.5 μN	37.5 μN	75 μN	187.5 μN	375 μN
0.8	2.95 μN	5.9 μN	29.5 μN	59 μN	147.5 μN	295 μN
0.6	2.1 μN	4.2 μN	21 μN	42 μN	105 μN	210 μN
0.4	1.25 μN	2.5 μN	12.5 μN	25 μN	62.5 μN	125 μN

4.2.4.3 Approximation Equations

Results and sliding inception points well correlate with the results of Etsion et al. [20] for a body defined by spherical surface which is the radius of curvature 1 configuration of this study as shown in Figure 4.7. There is a small shift in graphs which is acceptable by the authors up to 10% of error. This shift gets smaller for higher P^* values and almost same Q/P ratios are obtained at sliding inception. Sliding inception curve is also drawn in figure which is helpful to limit P^* values between selected values.

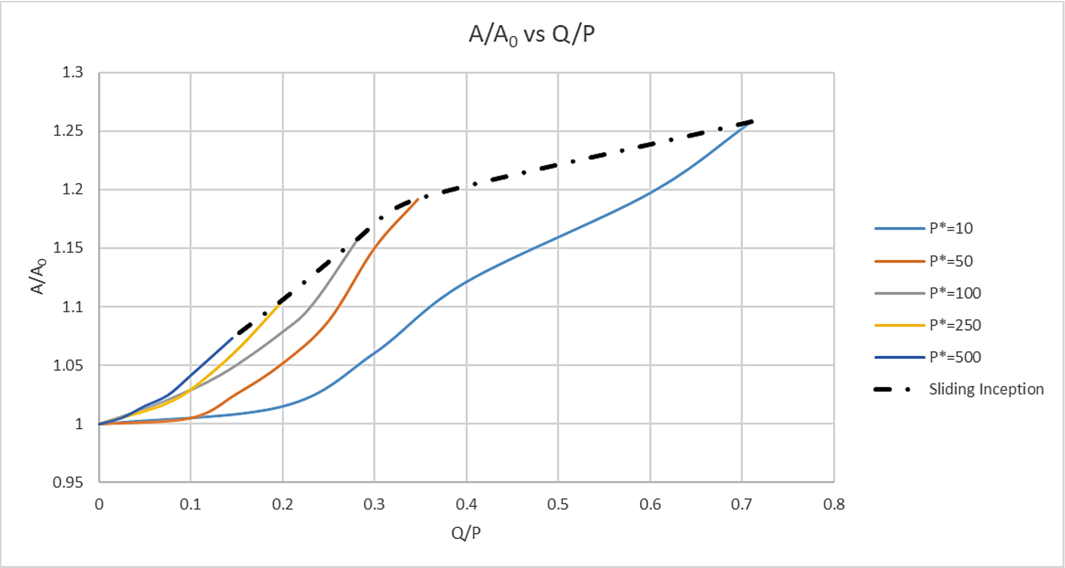

Figure 4.7 Junction growth and sliding inception of a body defined by spherical surface with sticking assumption

Junction growth for radius of curvature ratio of 1, until the sliding inception occurs can be approximated with the following non-dimensional equation which is based on curved surface parameters. 95.1% of the fitted results of the non-dimensional approximation Equation (4.4) is within 1.9% error. Additionally; proposed equation is also applicable down to radius of curvature ratio of 0.8. There are four different radius of curvature ratios investigated in this study. It is seen that instead of derivation of a single approximation equation, range between 0.8-1, 0.6-0.8 and 0.5-0.6 can be divided into three different approximation equations since, characteristics of junction growth differs as the radius of curvature ratio decreases.

$$\frac{A}{A_0} = 0.89 + \frac{\exp\left(P^{*^{\left(\frac{Q}{2.02P}\right)}} - 3.51\right)}{exp\left(-\frac{0.3R_x}{R_y}\right)} \qquad (4.4)$$

Similarly; junction growth for radius of curvature ratios of 0.5, 0.6 and 0.8 are shown in Figures 4.8, 4.9 and 4.10 respectively for changing P^* values of 10 to 500 with sticking assumption. It is seen that similar trends are observed but; “S” shape of trends become more visible as radius of curvature ratio reaches 0.5. Q/P ratios are nearly similar for different radius of curvature ratios when sliding inception takes place although load levels are quite different. In Figures 4.11 and 4.12, junction growth of radius of curvature ratios 1 and 0.8 are plotted using derived approximation equation. It is seen that the change in trends shows similarities.

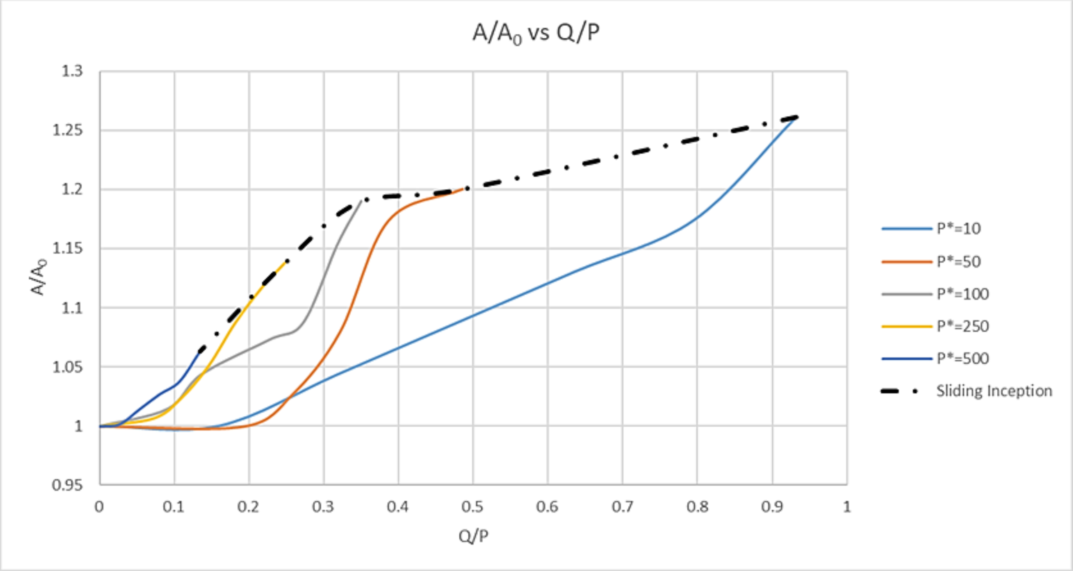

Figure 4.8 Junction growth and sliding inception of a body defined by curved surface with radius of curvature ratio of 0.5

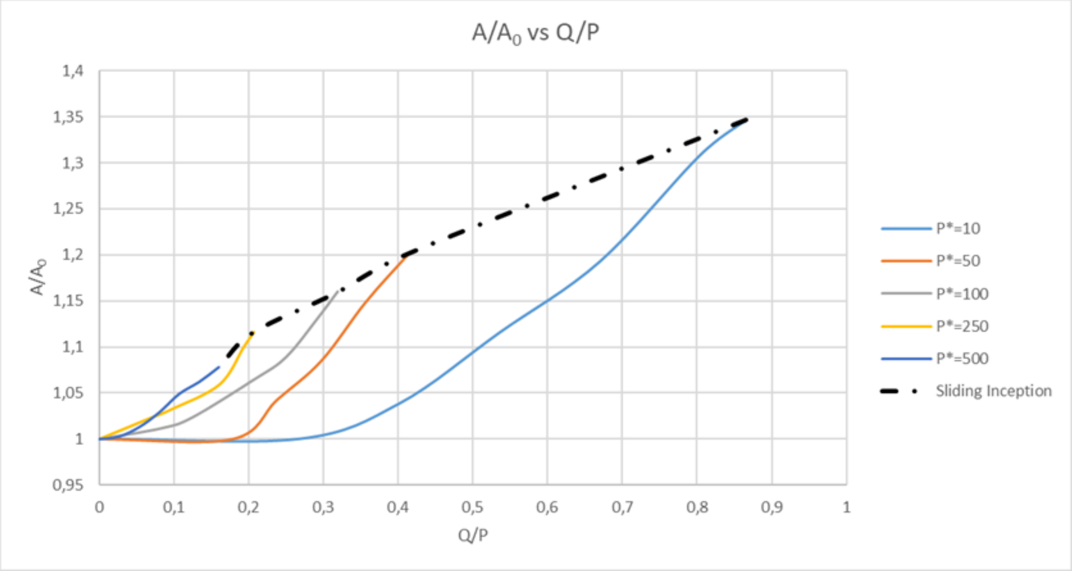

Figure 4.9 Junction growth and sliding inception of a body defined by curved surface with radius of curvature ratio of 0.6

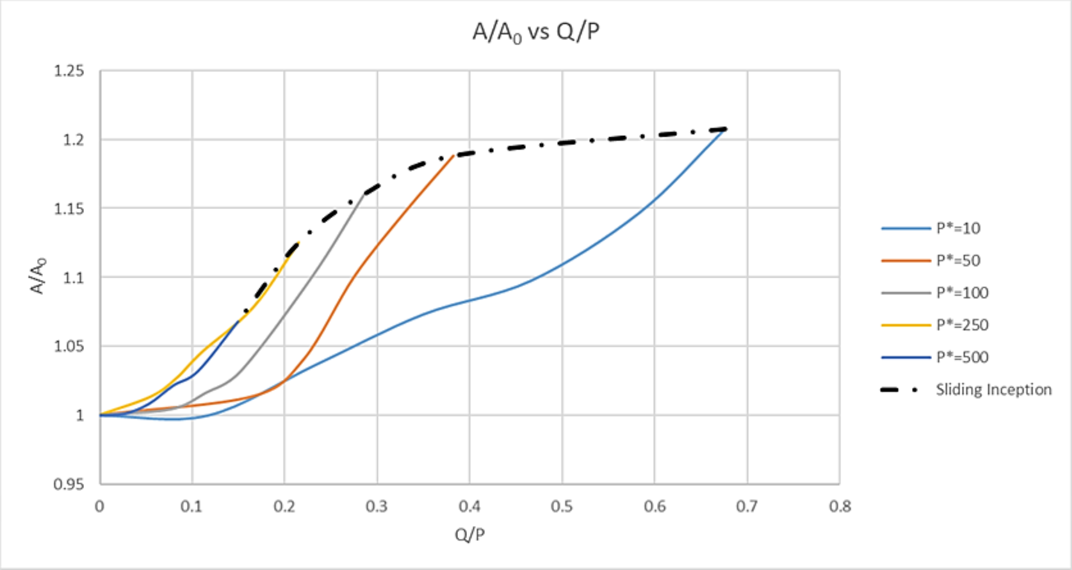

Figure 4.10 Junction growth and sliding inception of a body defined by curved surface with radius of curvature ratio of 0.8

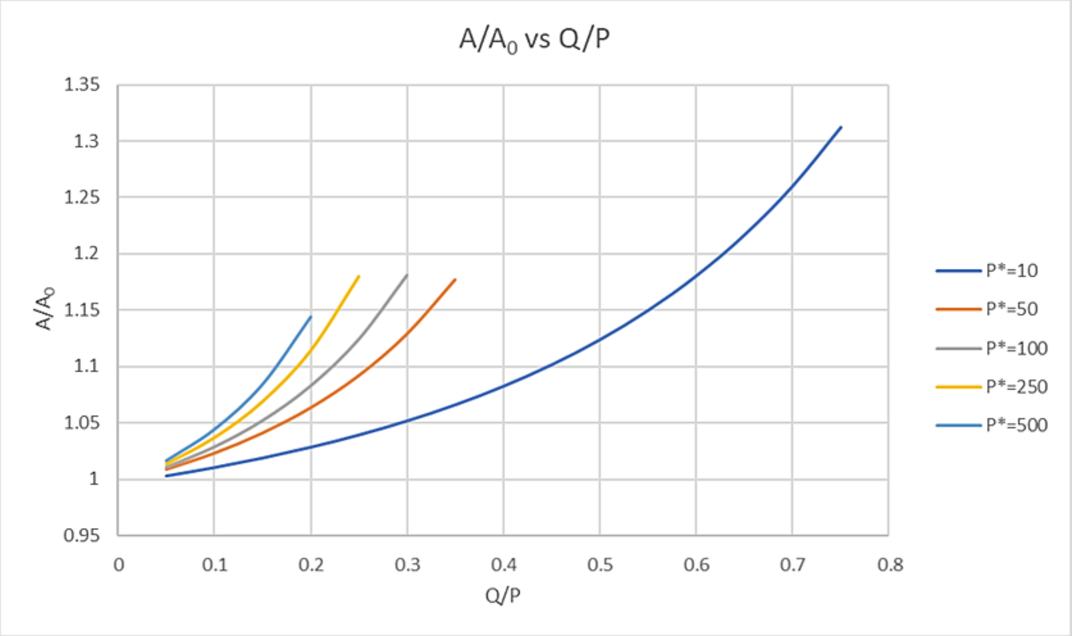

Figure 4.11 Junction growth equation of a body defined by curved surface with radius of curvature ratio of 1

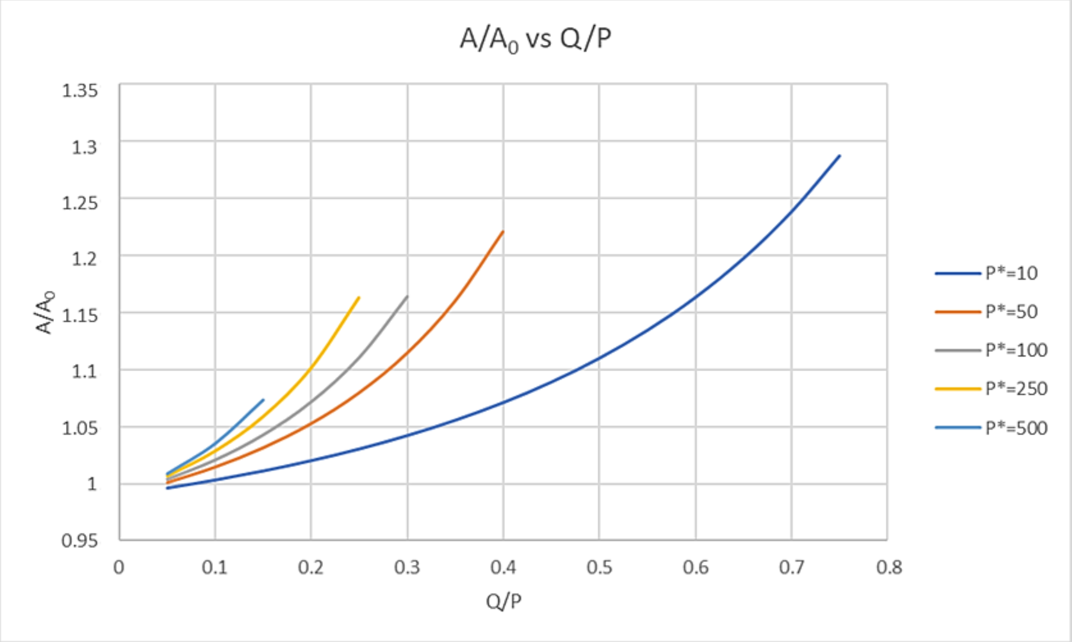

Figure 4.12 Junction growth equation of a body defined by curved surface with radius of curvature ratio of 0.8

Non-dimensional approximation Equation (4.5) is derived for radius of curvature ratio range 0.6-0.8 as the following. 93.8% of the fitted results of the non-dimensional approximation equation is within 2.1% error. In Appendix A, junction growth of radius of curvature ratio range 0.6-0.8 is plotted using derived approximation equation.

$$\frac{A}{A_0} = 0.89 + \frac{\exp\,[P^{*(\frac{Q}{2.13P})} - 3.46]}{exp\,(-\frac{0.28R_x}{R_y})} \tag{4.5}$$

Non-dimensional approximation Equation (4.6) is derived for radius of curvature ratio range 0.5-0.6 as the following. 97% of the fitted results of the non-dimensional approximation equation is within 3.6% error. In Appendix B, junction growth of radius of curvature ratio range 0.5-0.6 is plotted using derived approximation equation.

$$\frac{A}{A_0} = 0.87 + \frac{\exp\,[P^{*(\frac{Q}{2.55P})} - 3.64]}{exp\,(-\frac{1.05R_x}{R_y})} \tag{4.6}$$

Dotted lines in figures representing sliding inception give important information about the maximum junction growth for a specific radius of curvature and Q/P ratio. Maximum A/A_0 must be limited by an equation which is the following. 90% of the fitted results of the non-dimensional approximation Equation (4.7) is within 2.4% error. Sliding inception of radius of curvature ratios of 0.4, 0.6, 0.8 and 1 are plotted in Figure 4.13 using derived approximation equation.

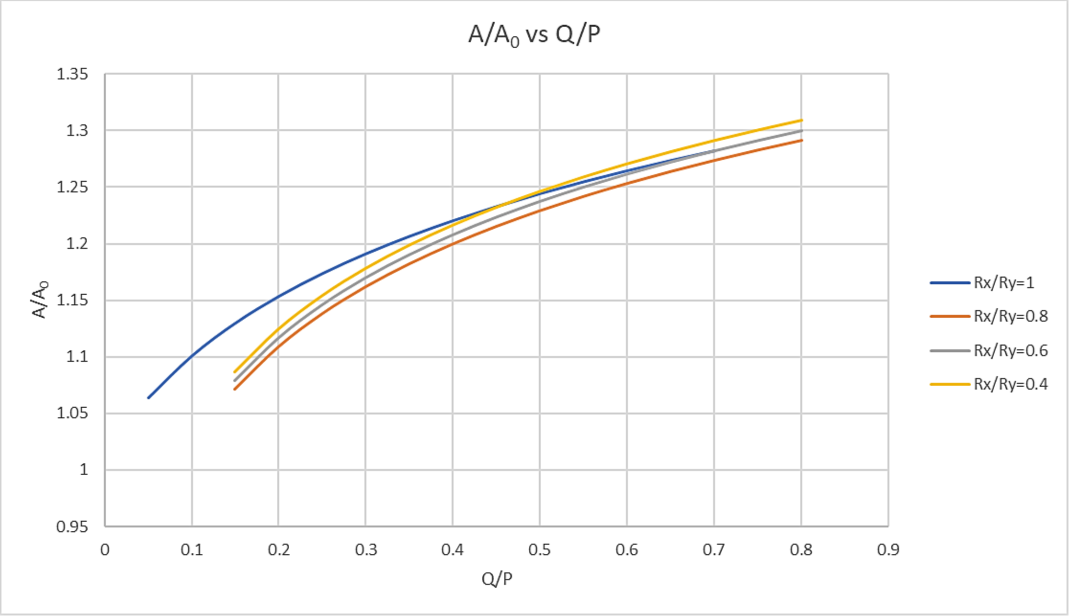

Figure 4.13 Sliding inception equation of bodies defined by curved surfaces with radius of curvature ratios of 0.4, 0.6, 0.8 and 1

$$\frac{A}{A_0} = \frac{\exp\left[1.31 - (\frac{Q}{P})^{-0.1}\right]}{1 + \frac{1}{28.17}(\frac{R_x}{R_y})} \tag{4.7}$$

As noted, measured surface roughness is converted to 3D bodies where the derived approximation equations are used. In cases of irregular shapes, formulation proposed by Tabor [16] is used to calculate junction growth which is the following for large preloads;

$$\frac{A}{A_0} = \sqrt{1 + \alpha(\frac{Q}{P})^2} \tag{4.8}$$

Another formulation is proposed by Etsion et al. [20] that gives a better approximation for smaller preloads such as $P^* = 1$. Empirical expression proposed is the following which is derived independent of material;

$$\frac{A}{A_0} = 1 + 0.6(\frac{Q}{P})^4 \tag{4.9}$$

4.2.5 Solid (Real) Contact Area Ratio

In rough surface contact, solid contact occurs at highest surface peaks which corresponds to a smaller surface than projected area. As the normal load increases, this solid contact area also increases while more asperities come into contact to support load. Since lubricant effects are excluded, a relation can be found between the normal load and the solid (real) contact area for a measured real surface roughness. Volume conservation effects are also included in the simulation which accounts for surface rise. There is no need to balance the deformed area with rising non-contacting surface.

Since it is a time-consuming work to digitize whole surface of blank to be used, a repeating pattern of a surface roughness is selected to be investigated. An area of 0.32 x 0.32 mm (quarter of the measured area) is generated with 228 x 228 nodes and modeled as a cubic body as shown in Figure 4.14. One of the six surfaces is made of real surface roughness while other surfaces are smooth and restricted to move with boundary conditions. Maximum mesh size of the rough surface is limited to 4 μm. Inflation meshing method is used with 5 layers of mesh located in the vicinity of the rough surface in order to capture effects of small deformations. Using multiple layers helps to capture gradients on wall like structures similar to deformed body in this study but increases node number and simulation time significantly. Deformable body is fixed from bottom surface in space. A rigid flat body is restrained to move in normal direction, without rotation, towards deformable body and side walls of the cube are restrained not to deform outside of the projected boundary. 75% of the distance from highest node to lowest node in normal direction, is deformed to have interpolation data between solid (real) contact area and normal load. Rigid body velocity is kept same in order to avoid effects of different strain rates in results.

3D roughness is deformed by a rigid flat constraint to move in normal direction. Solid (real) contact area with rigid body movement at 0.3 μm depth is shown in Figure 4.15. Solid contact area is calculated by the nodes where pressure readings are positive. It is seen that as the deformation increases, valleys between peaks become smaller and isolated. It is the main characteristics of boundary lubrication that lubricants are trapped in similar zones that is observed.

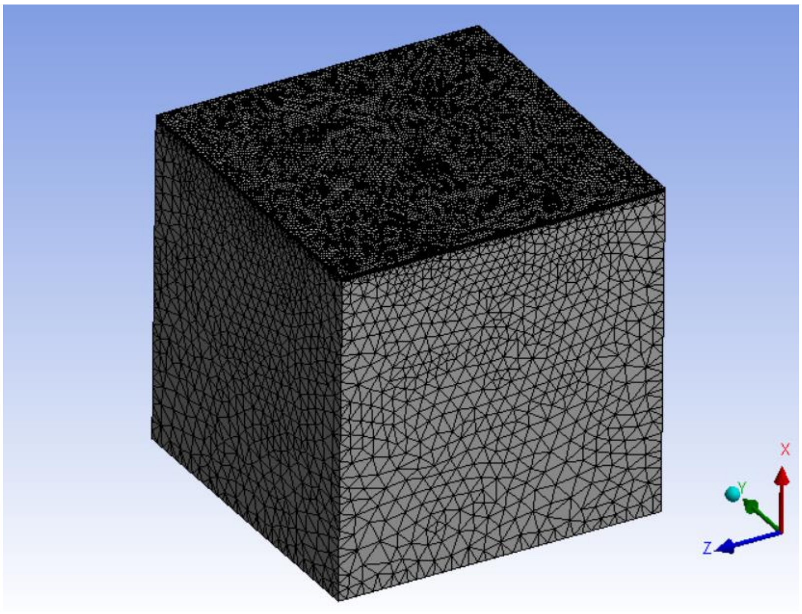

Figure 4.14 FEM of measured 3D roughness (0.32 x 0.32 mm)

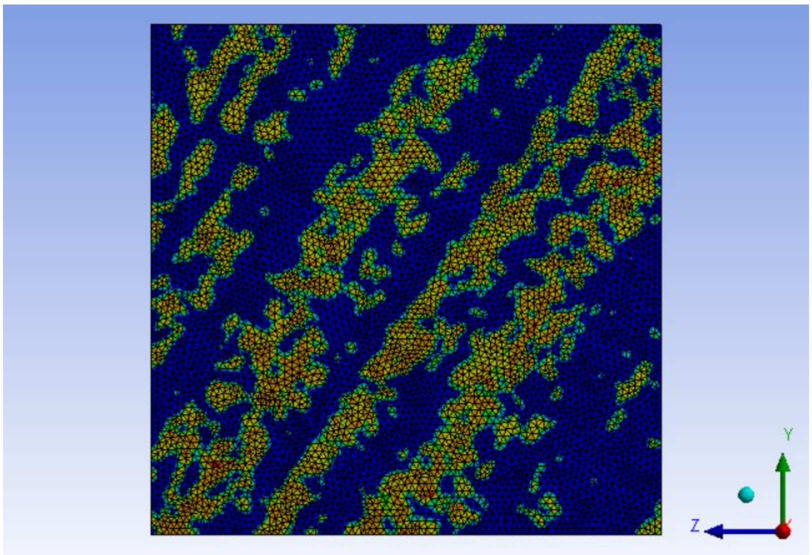

Figure 4.15 Solid contact area after deformation of measured surface roughness

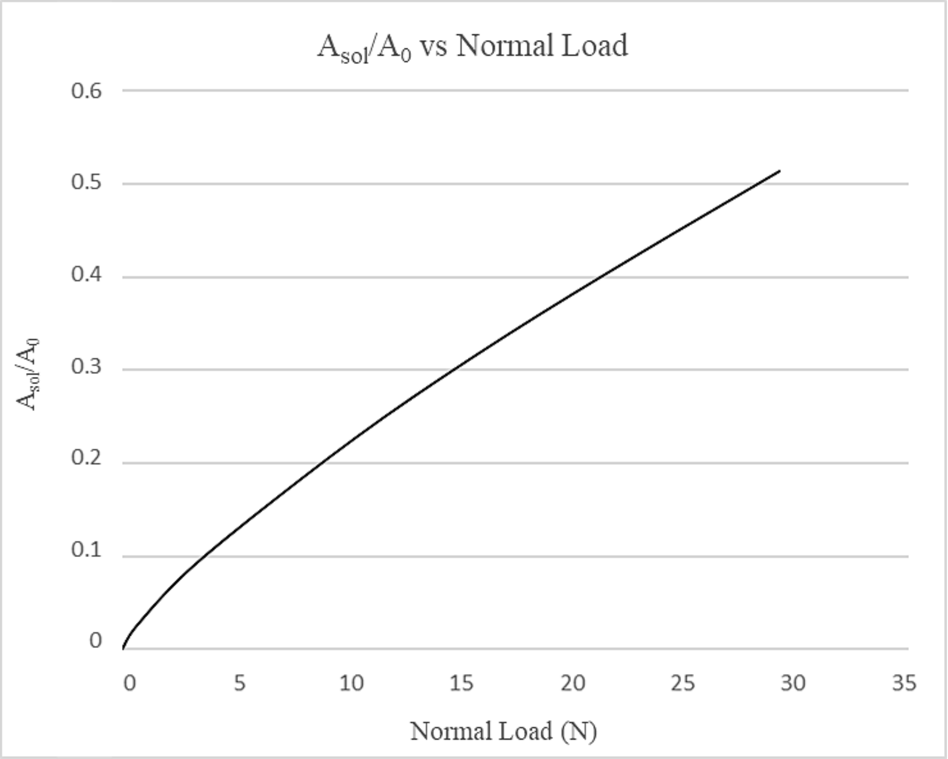

Figure 4.16 Solid contact area ratio change with respect to normal load

Solid (real) contact area ratio change with respect to increasing normal load is shown in Figure 4.16. It is seen that as the normal deformation increases, there is more contact area to deform and a linear increasing trend is observed. Solid (real) contact area reaching 30% of the projected area requires 15 N. This type of data is useful to relate how much load is required to deform a specific roughness for a limited surface area.

4.2.6 Lubrication Model

Reynolds equation is solved for pressure and shear flow factors separately. In order to solve pressure flow factor, surfaces are assumed to be stationary ($\boldsymbol{u}_1 = \boldsymbol{u}_2 = 0$ and surface separation is constant ($\partial h/\partial t = 0$). Then; substituting parameters into the general equation reduces to following equations in planar domain for pressure flow factor and shear flow factor respectively [3];

$$\frac{\partial}{\partial x}\left(\frac{h^3}{12\eta}\frac{\partial P}{\partial x}\right)+\frac{\partial}{\partial y}\left(\frac{h^3}{12\eta}\frac{\partial P}{\partial y}\right)=0 \tag{4.10}$$

$$\frac{\partial}{\partial x}\left(\frac{h^3}{12\eta}\frac{\partial P}{\partial x}\right)+\frac{\partial}{\partial y}\left(\frac{h^3}{12\eta}\frac{\partial P}{\partial y}\right)=\frac{\partial h}{\partial t} \tag{4.11}$$

$\partial h/\partial t$ can be re-written in terms of U_s and Δx as the following;

$$\frac{\partial h}{\partial t}=\frac{U_s}{2\Delta x}\left[h(x,y,t+\Delta t/2)-h(x,y,t-\Delta t/2)\right] \tag{4.12}$$

where Δx is the resolution of the rough surface which is also the minimum movement which can be calculated by film thickness change. Then; by finite difference $h(x,y,t+\Delta t/2)$ and $h(x,y,t-\Delta t/2)$ can be written as;

$$h(x,y,t+\Delta t/2) = (h_T + \delta_{1-} + \delta_{2+}) \tag{4.13}$$

$$h(x,y,t-\Delta t/2) = (h_T + \delta_{1+} + \delta_{2-}) \tag{4.14}$$

where;

$\delta_{1-} = \delta_1(x - \Delta\mathrm{x}/2, \mathrm{y}, \mathrm{t})$

$\delta_{2-} = \delta_2(x - \Delta\mathrm{x}/2, \mathrm{y}, \mathrm{t})$

$\delta_{1+} = \delta_1(x + \Delta\mathrm{x}/2, \mathrm{y}, \mathrm{t})$

$\delta_{2+} = \delta_2(x + \Delta\mathrm{x}/2, \mathrm{y}, \mathrm{t})$

Finite difference solution method is used in order to solve pressure flow factor, nodal equations can be transformed into the following structure [3];

$$A_{iN}P_{iN} + A_{iS}P_{iS} + A_{iE}P_{iE} + A_{iW}P_{iW} - A_{iP}P_{iP} = 0, \quad i = 1,2,\dots,m \tag{4.15}$$

where;

$A_{iN} = k_{in}\dfrac{\Delta x}{\Delta y}$

$A_{iS} = k_{is}\dfrac{\Delta x}{\Delta y}$

$A_{iE} = k_{ie}\dfrac{\Delta x}{\Delta y}$

$A_{iW} = k_{iw}\dfrac{\Delta x}{\Delta y}$

and

$A_{iP} = A_{iN} + A_{iS} + A_{iE} + A_{iW}$

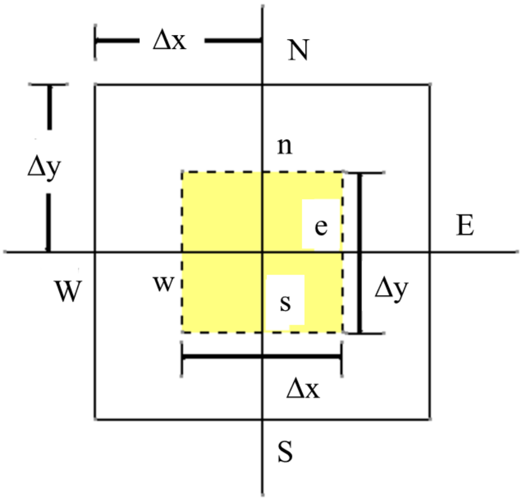

Figure 4.17 Schematic view of neighboring nodes N, E, W and S [3]

Naming and positioning of the neighboring nodes are shown in Figure 4.17. When resolution of the rough surface is selected to be Δx = Δy then, harmonic mean is used to calculate coefficients (k) in adjacent nodes;

$$k_{in} = \frac{2}{\frac{1}{k_{iN}} + \frac{1}{k_{iP}}}$$

$$k_{is} = \frac{2}{\frac{1}{k_{iS}} + \frac{1}{k_{iP}}}$$

$$k_{ie} = \frac{2}{\frac{1}{k_{iE}} + \frac{1}{k_{iP}}}$$

$$k_{iw} = \frac{2}{\frac{1}{k_{iW}} + \frac{1}{k_{iP}}}$$

and

$$k_{iN} = h_{iN}^3, \quad k_{iS} = h_{iS}^3, \quad k_{iE} = h_{iE}^3, \quad k_{iW} = h_{iW}^3, \quad k_{iP} = h_{iP}^3 \tag{4.16}$$

For the shear flow factor, B_{iP} is added to RHS of the general equation.

$$A_{iN}P_{iN} + A_{iS}P_{iS} + A_{iE}P_{iE} + A_{iW}P_{iW} - A_{iP}P_{iP} = B_{iP}, \quad i = 1,2, \dots, m \tag{4.17}$$

Then; A terms will remain the same while B_{iP} is calculated for each node from the following;

$$B_{iP} = 12\eta(\frac{\partial h}{\partial t})_{\mathrm{i}p} \tag{4.18}$$

4.2.7 Asperity Ploughing Model

Last step of coefficient of friction calculation is the determination of the total shear stress. Total shear stress is the summation of shear stress of all asperity contacts (τ_{sol}) and lubricant shearing (τ_{lub}) due to lubricant pressure gradient and relative velocities of surfaces. τ_{sol} is calculated in two deformation levels. In first stage workpiece softer asperities are flattened by rigid tool surface then; harder and small-scale tool asperities plough through the flattened areas of asperities. Schematic representation of two stage asperity ploughing model is shown in Figure 4.18.

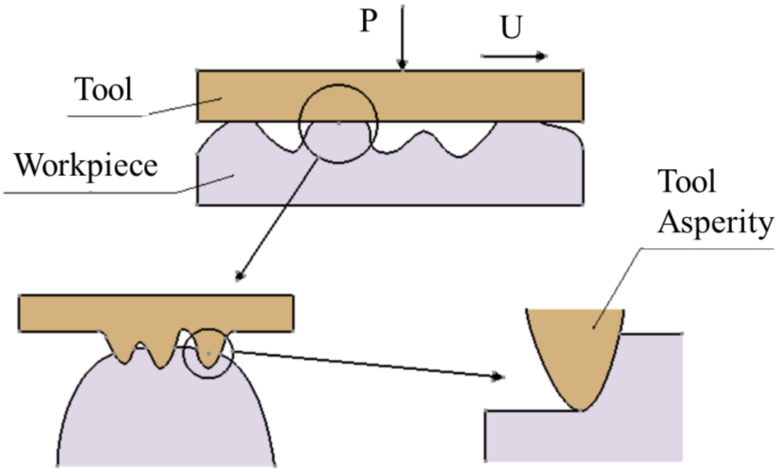

Figure 4.18 Flattened workpiece asperities ploughed by tool asperities

In literature, tool asperities that penetrate and plough through the deformable workpiece material called contact patches [39,40,41,42]. In every flatten asperity tip at interface, there may be multiple contact patches due to asperity distribution on tool surface. Asperity heights as bars in these contact patches are fitted to elliptical bodies as proposed by Rooij [40]. Schematic representation of contact patches composed of asperity height bars are shown in Figure 4.19.

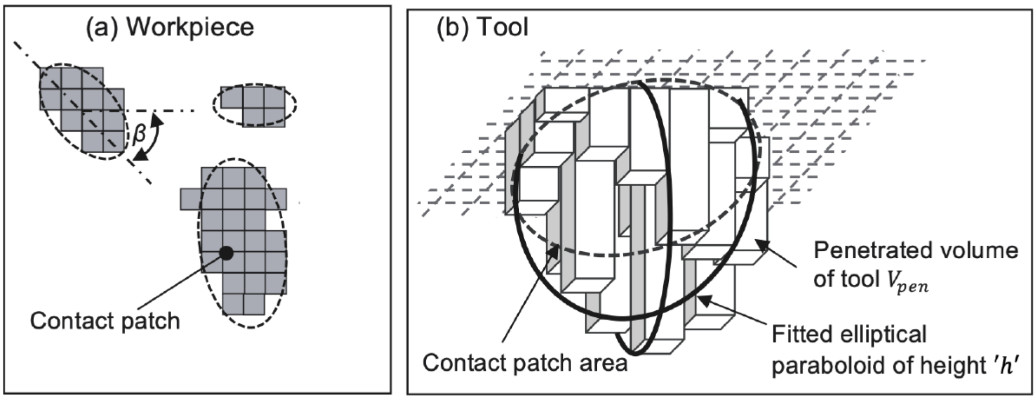

Figure 4.19 Contact patches and elliptical body fitting [42]

Equations are not available for ploughing of rigid asperites defined by curved surfaces with variable attack angles. Therefore; shear stress due to ploughing of rigid asperities are tabularized with rough mesh simulations since precise nodal values are not needed and high number of simulations with different configurations. The mechanism of the shear stress generated due to ploughed asperities is composed of two parts. First part is the force generated due to hardness of the deformed material and the projection area of ploughing asperities. Second part is the shearing of the lubricant at whole contact interface of the ploughed asperity and deformed material. Boundary lubrication is assumed and reference values are taken from literature for a commercial lubricant. Shear stress is composed of two parts, front projection area and hardness of workpiece material cause first part and lubricant shear due to flowing workpiece material around indented body with a certain indentation depth. τ_{BL} is used in calculations which is the result of experiments carried for Fuchs Anticorit PLS100T lubricant [43]. It is measured for a specific material and lubricant and since this study does not include experimental applications, an already measured boundary lubrication shear stress value in literature is used as reference. Lubricant boundary shear stress is calculated as;

$$\tau_{BL} = c_0 p_0^m \tag{4.19}$$

where; $c_0 = 7.34$ and $m = 0.78$ for Fuchs Anticorit PLS100T lubricant. p_0 is obtained by dividing the normal load with the real solid-to-solid contact area, which is;

$$p_0 = P/A_{sol} \tag{4.20}$$

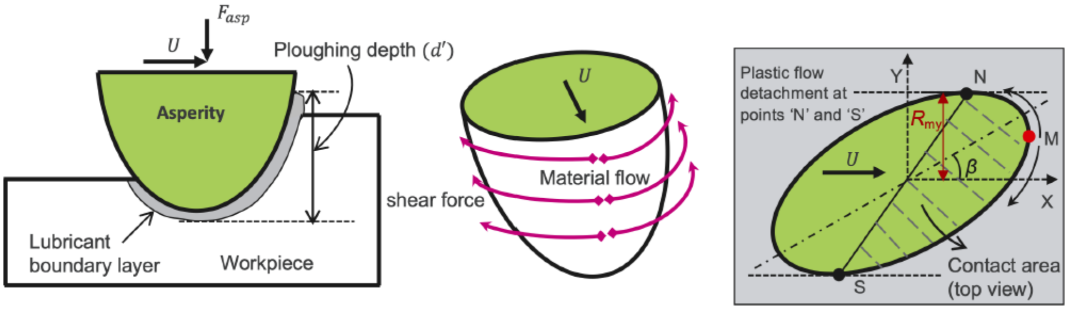

Figure 4.20 Asperity ploughing model [42]

Combined loading is applied in all cases which is gradually applied normal load is followed by a gradually increased tangential load when maximum is reached. When only normal load is applied by tooling surface, indented asperities at contact patches balance the force. When tangential load increases up to a limit and relative movement or sliding starts, only frontal half of the indented rigid asperities carry normal load as seen from Figure 4.20. It is a common approach in literature that the contact area decreases half and contact area must be enlarged to carry normal load. More indentation is required to increase solid contact area to two times.

As shown in Figure 4.21, tool asperity defined by a curved surface and with an attack angle is modeled at a fixed indentation depth. Workpiece is deformable and tool asperities is assumed to be rigid. In order to be realistic, deformable workpiece is modeled with a cavity in the form of tool asperity. Then; tool asperity is forced to move into the deformable workpiece to plow through without load calculations. Shear stresses are read from simulation results when contact status change into sliding. Tangential force (in sliding direction) is read when average shear stress at contact interface is equal to τ_{BL}.

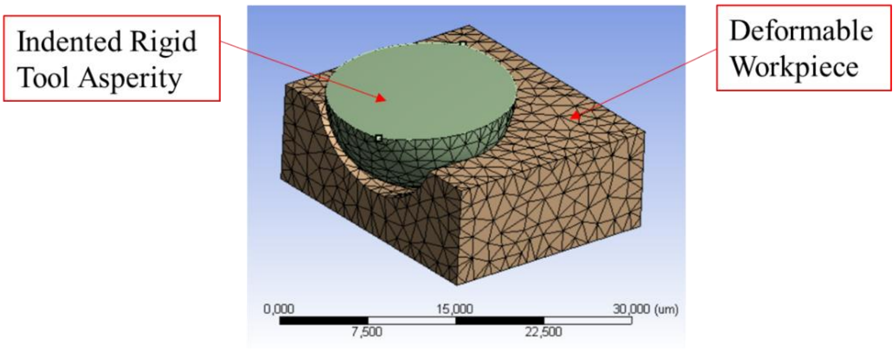

Figure 4.21 Tool asperity ploughing with attack angle FEM model

4.2.8 Coefficient of Friction Calculation

There are three different interfaces that occur during a deep drawing simulation which are punch-blank, die-blank and blank holder-blank interfaces. A constant coefficient of friction needs to be determined per interface throughout the deep drawing process. Steps of solving the coefficient of friction at every 5 mm step of deep drawing simulation for 0.64 x 0.64 mm contact regions for all interfaces are summarized in the flow chart.

Total shear force is composed of summation of the shear forces generated by solid-to-solid contact and shear force of lubricant at workpiece surface. Since projected contact area is not same as the solid contact area, total shear stress is calculated from the following;

$$F_S = F_{sol} + (1 - A_{sol})\tau_{lub} \tag{4.21}$$

Shear stress created by solid contact is calculated from interpolation data created from FEM simulations. Shear stress from lubricant is calculated by the equation proposed by Hamrock et al. [44] for a Newtonian fluid;

$$\tau_{lub} = \eta \frac{(v_2 - v_1)}{h_{avg}} - \frac{h_{avg}}{2} \Delta P_{lub} \tag{4.22}$$

Finally; coefficient of friction is calculated by dividing the total shear force to the normal contact load as the following;

$$f = \frac{F_s}{P} \tag{4.23}$$

4.2.9 Friction Model Flow Chart

Flow chart to be followed starting from simulations and 3D measurements up to calculation of coefficient of friction is summarized in Figure 4.22.

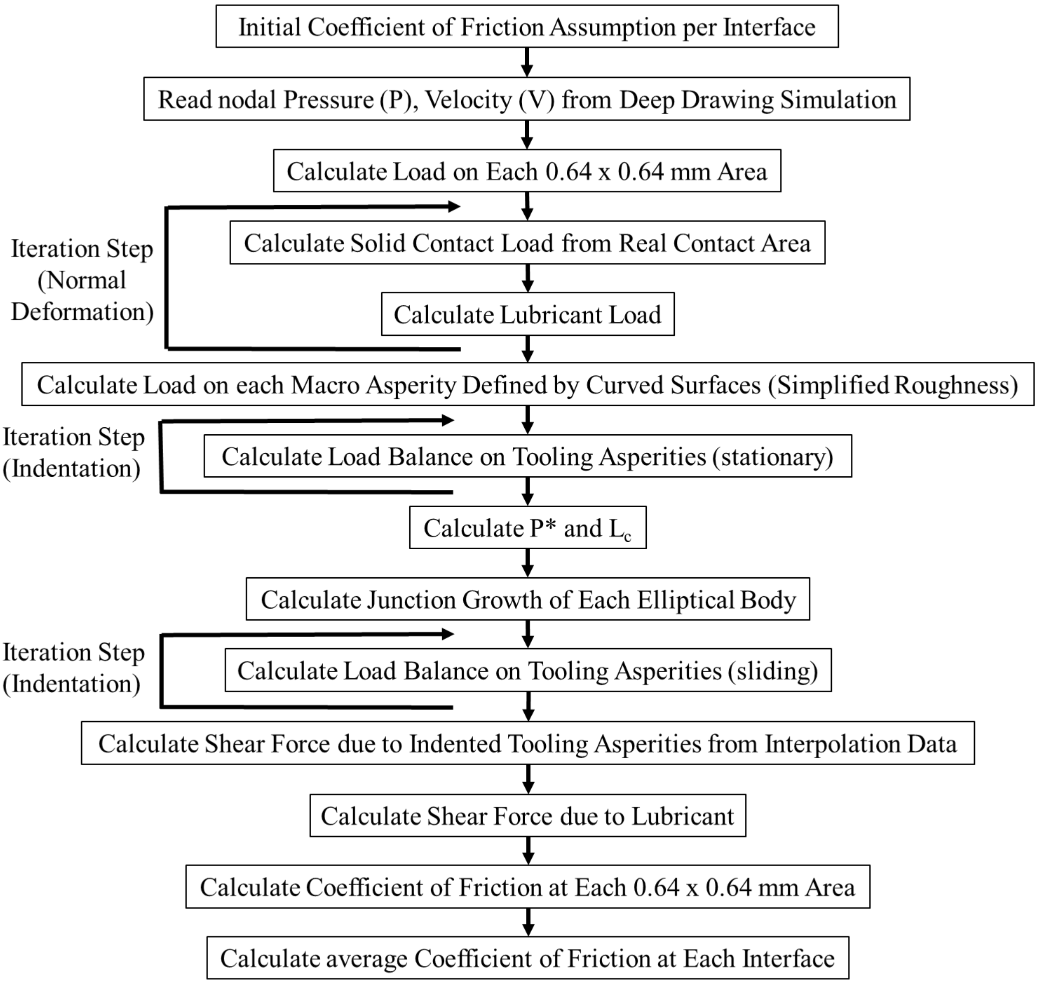

Figure 4.22 Flow chart of the friction model

CHAPTER 5

RESULTS AND DISCUSSION

A steel blank made of DKP6112, with 100 mm diameter and 1 mm thickness, deep drawn to a 35 mm cylindrical cup. Tool and blank components of a cylindrical cup drawing process is shown in Figure 5.1. Deep drawing tool and blank dimensions are adapted from Dizeci [36] and shown in Figure 5.2. Simulations are performed for the adapted geometry and results of the friction model are presented throughout the chapter.

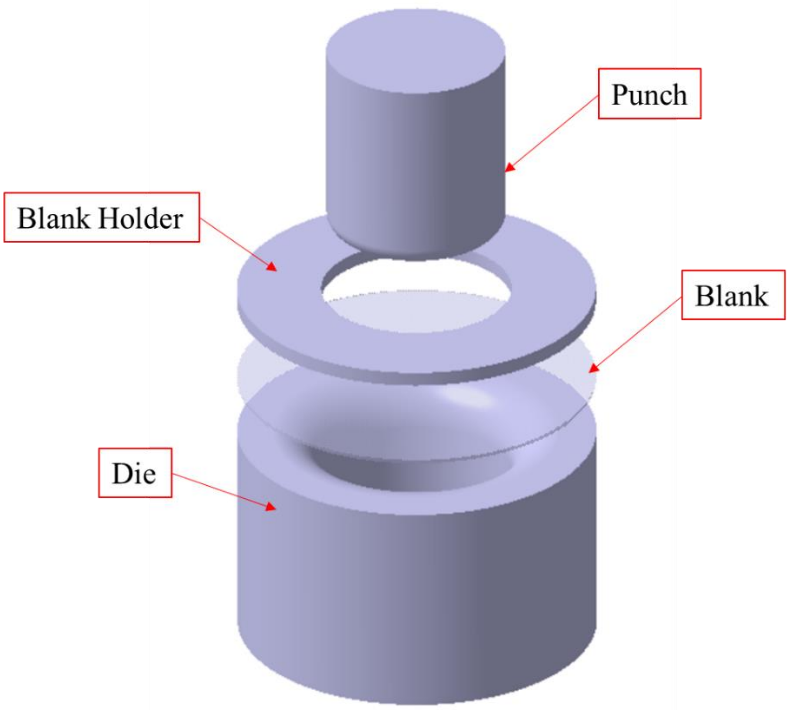

Figure 5.1 Deep drawing tool and blank geometries

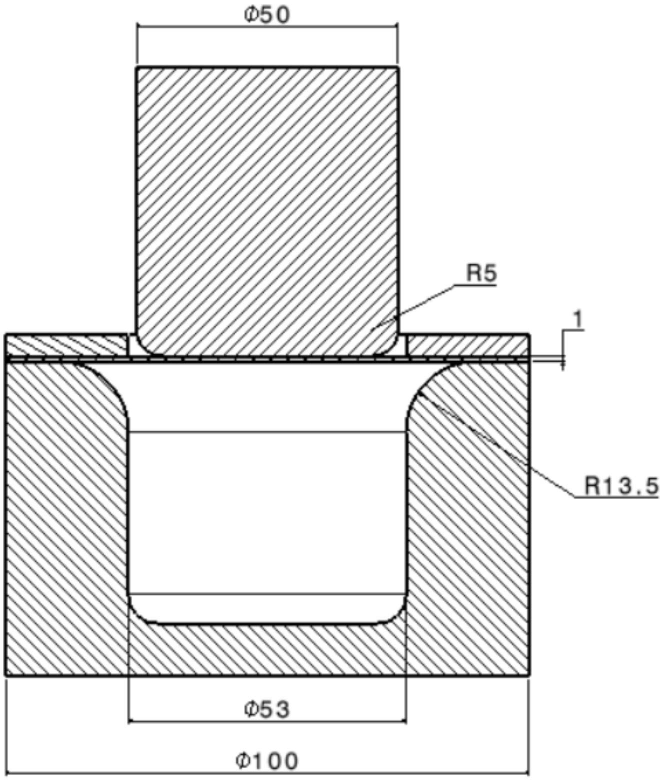

Figure 5.2 Deep drawing punch, die, blank holder and blank geometry (dimensions in mm)

At every 5 mm height coefficient of friction is calculated at each 0.64 x 0.64 mm region along the radial direction as shown in Figure 5.3. Then; average coefficient of friction is set to each interface (blank-die, blank-blank holder and blank-punch) and simulation restarts until next increment. After 7 stages, deep drawing process is completed and strain resuls are presented.

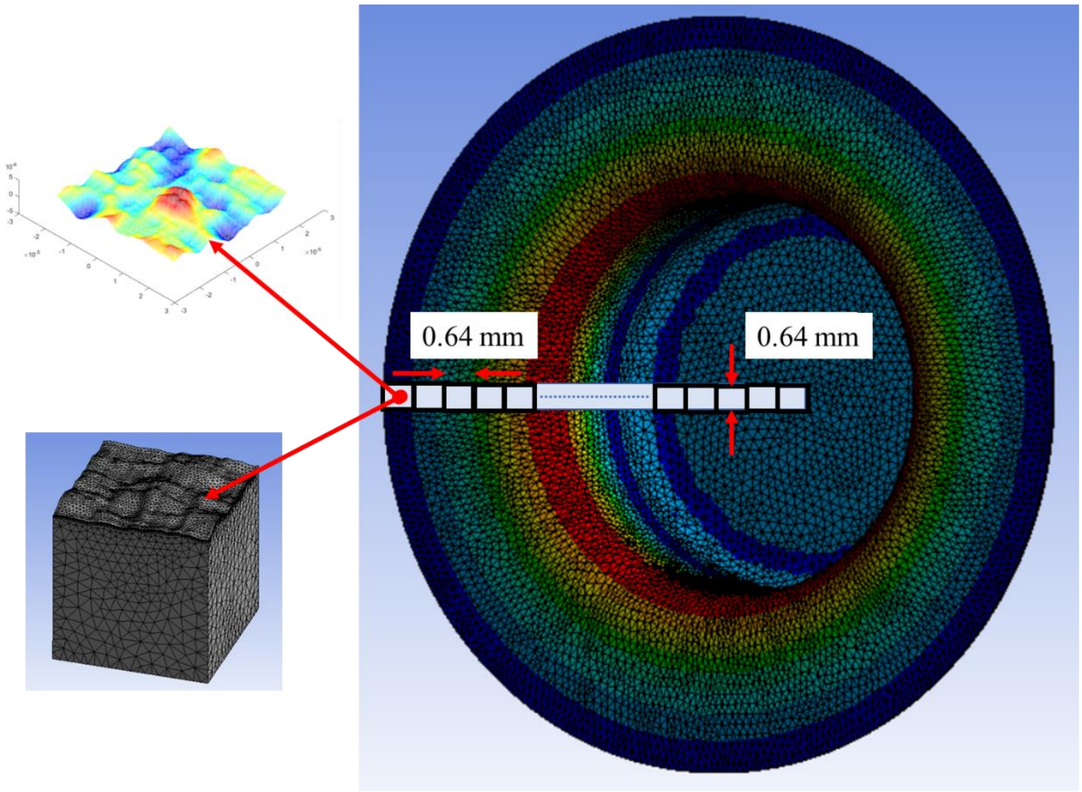

Figure 5.3 Schematic distribution of 0.64 x 0.64 mm regions on deep drawn part to be investigated with measured roughness

In order to represent real life conditions, the measurements are taken from blank by an optical 3D surface roughness measurement instrument. After applying the steps given in the flow chart which is shown in previous chapter, average coefficient of friction is calculated for each interface. Results of the average coefficient of friction are summarized in Table 5.1 for cup height steps until 35 mm final cup height is reached.

Table 5.1 Average coefficient of friction for blank-punch, blank-blank holder and blank-die interfaces

Cup Height (mm)	*5*	*10*	*15*	*20*	*25*	*30*	*35*
Blank-Punch	0.260	0.247	0.248	0.252	0.263	0.265	0.267
Blank-B. Holder	0.300	0.298	0.292	0.276	0.253	0.250	0.273
Blank-Die	0.305	0.301	0.291	0.273	0.264	0.244	0.241

Outputs of simulation are used to perform nodal calculations for coefficient of friction. Both surfaces of the blank are treated separately as punch side and die side. Pressure distribution on nodes at symmetry plane for 15 mm, 25 mm and 35 mm cup heights are shown in Figure 5.4 for punch side of the blank. As seen from figure, pressure is almost zero at the punch nose contact area and zero at the gap between die and punch. Highest pressures are observed at the punch radius contact area where the blank is deformed into a cup. Pressure values are smaller for 15 mm cup height and almost similar values are read for 25 mm and 25 mm cup heights around 150 MPa. At the blank holder contact region, blank deforms and drawn into the die opening which decreases contact length as the cup height increases. Since; same blank holder clamping force is kept constant, smaller contact area results in very high pressure values for 35 mm cup height.

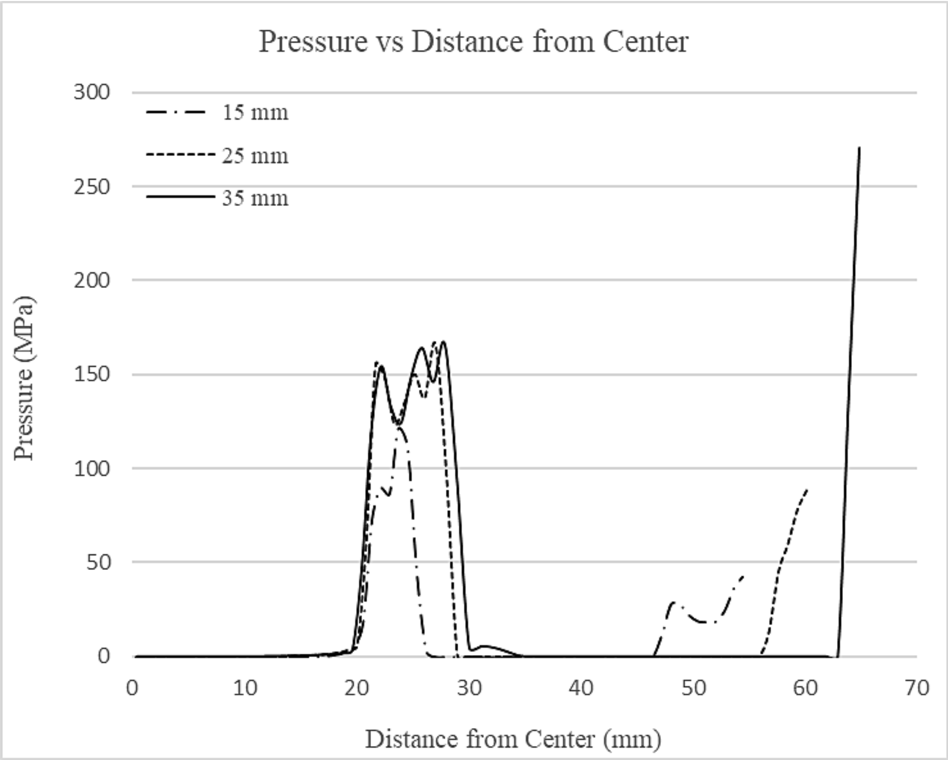

Figure 5.4 Pressure distribution on nodes at symmetry plane for 15 mm, 25 mm and 35 mm cup heights (punch side)

0.64 x 0.64 mm regions are considered in calculations therefore; normal load on the areas of interest are obtained from pressure distribution. Pressure distribution is assumed to be similar to piecewise function. Load distribution calculated from the pressure distribution on 0.64 x 0.64 regions at symmetry plane for 15 mm, 25 mm and 35 mm cup heights are shown in Figure 5.5 for punch side of the blank. As seen from figure, average contact load at the punch radius contact area increases as the cup height increases from 15 mm to 25 mm. Similar to 25 mm cup height load distribution, 35 mm values are similar like the pressure distribution which varies between 55-70 N.

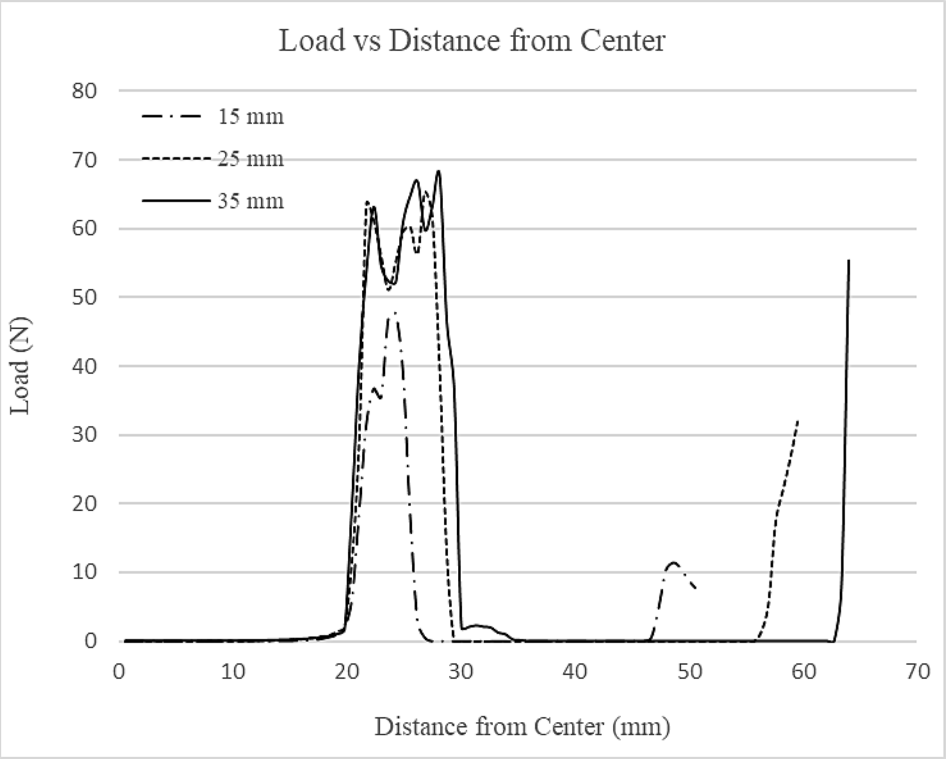

Figure 5.5 Load distribution on 0.64 x 0.64 regions at symmetry plane for 15 mm, 25 mm and 35 mm cup heights (punch side)

Local coefficients of friction are calculated over the whole symmetry axis for blank-punch and blank-blank holder interfaces. Steps in the flow chart are performed and coefficient of friction distribution on 0.64 x 0.64 mm regions at symmetry plane for 15 mm, 25 mm and 35 mm cup heights are shown in Figure 5.6. As seen from figure, coefficients of friction vary between 0.2 and 0.3 independent of the contact load variation. Coefficient of friction is highly dependent on the type of lubricant and boundary shear strength generated at the interface. Blank holder contact region has a very sharp change with irregular distribution. Contact area changes drastically and coefficient of friction changes between 0.2-0.3 while, value is almost 0.3 for cup height of 15 mm.

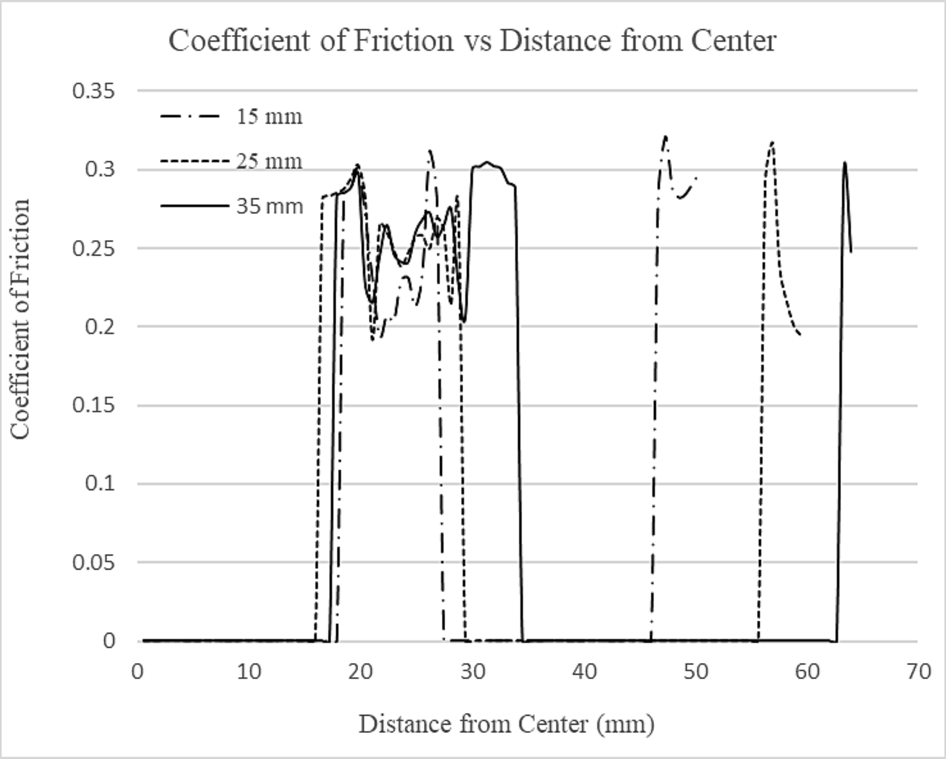

Figure 5.6 Coefficient of friction distribution on 0.64 x 0.64 regions at symmetry plane for 15 mm, 25 mm and 35 mm cup heights (punch side)

Similar to punch side, pressure distribution on nodes at symmetry plane for 15 mm, 25 mm and 35 mm cup heights are shown in Figure 5.7 for die side of the blank. As seen from figure, length of contact between die and blank becomes longer as the drawn part elongates during process. Similar pressure values are observed for 15 mm and 25 mm cup dephts while, more than 2.5 times of the pressure values are read for 35 mm cup height. General trend in pressure change is that, pressure is high at the beginning of the die radius contact region and decreases until the end of the radius where a minima is seen. Then; flat region of the die starts which results in increase of contact pressure due to blank holder clamping force.

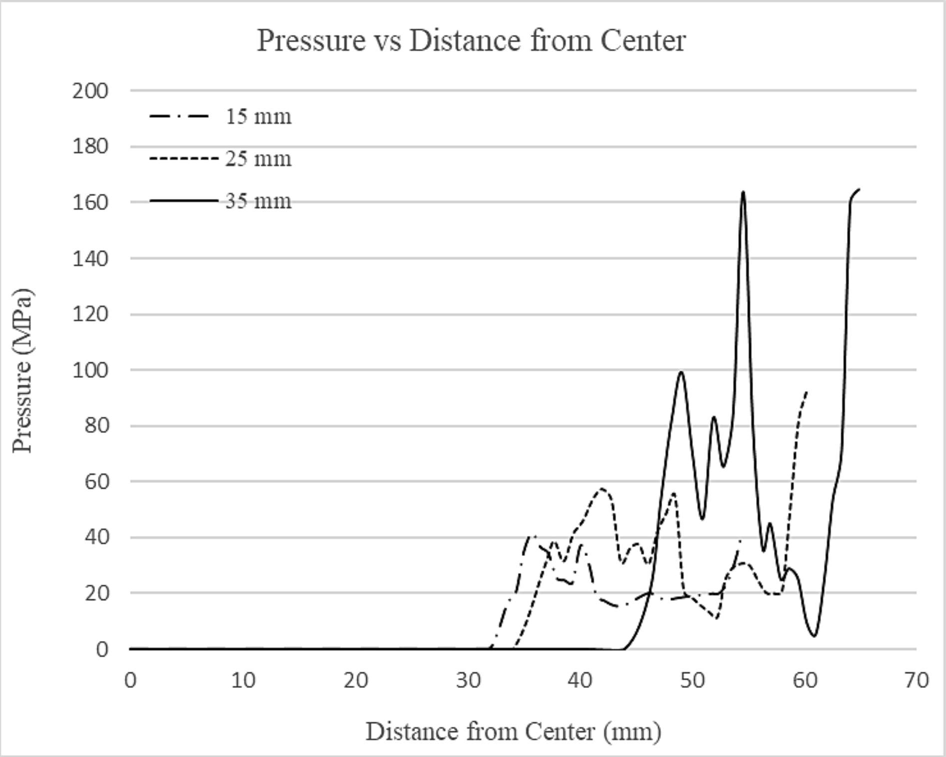

Figure 5.7 Pressure distribution on nodes at symmetry plane for 15 mm, 25 mm and 35 mm cup heights (die side)

Load distribution on 0.64 x 0.64 regions at symmetry plane for 15 mm, 25 mm and 35 mm cup heights are shown in Figure 5.8 for die side of the blank. Similar distribution with pressure is observed. As seen from figure, load at the beginning and at the end of the die radius contact are similar for 15 mm and 25 mm cup heights. 3 times the maximum load of 15 mm and 25 mm cup heights are observed for 35 mm cup height. Also the minima observed at the end of the die radius contact is smallest for 35 mm cup height.

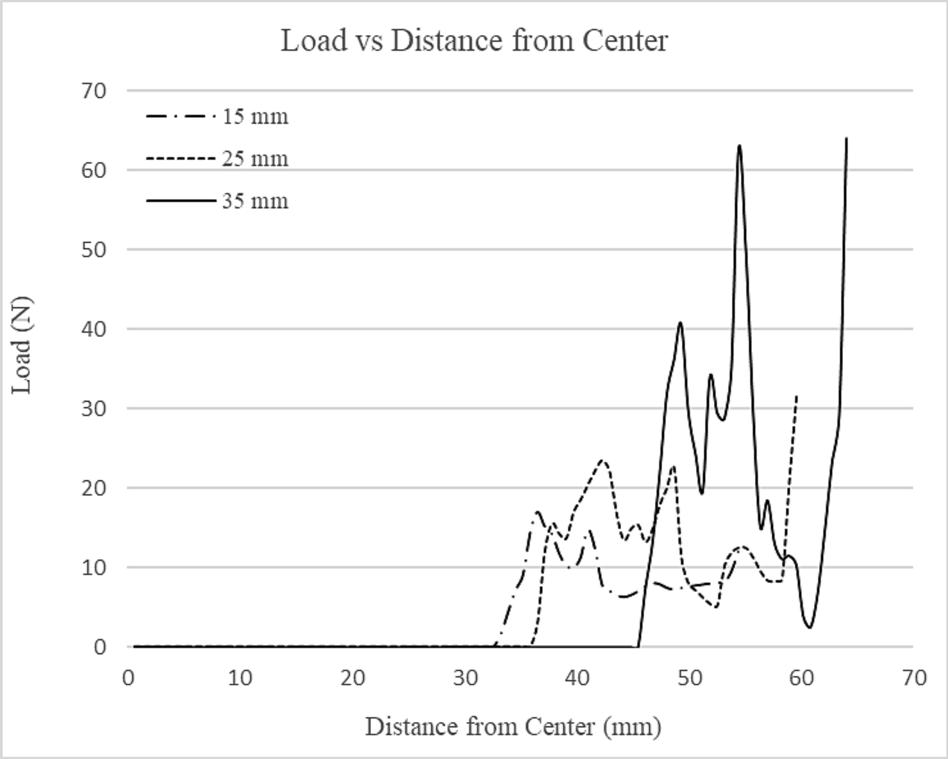

Figure 5.8 Load distribution on 0.64 x 0.64 regions at symmetry plane for 15 mm, 25 mm and 35 mm cup heights (die side)

Coefficient of friction distribution on 0.64 x 0.64 regions at symmetry plane for 15 mm, 25 mm and 35 mm cup heights are shown in Figure 5.9 for die side of the blank. Similar coefficient of friction range is observed with punch side of the blank. As the blank elongates, distance from center shifts in radial direction. Highest coefficient of friction values are calculated at beginning and end of the die radius contact region.

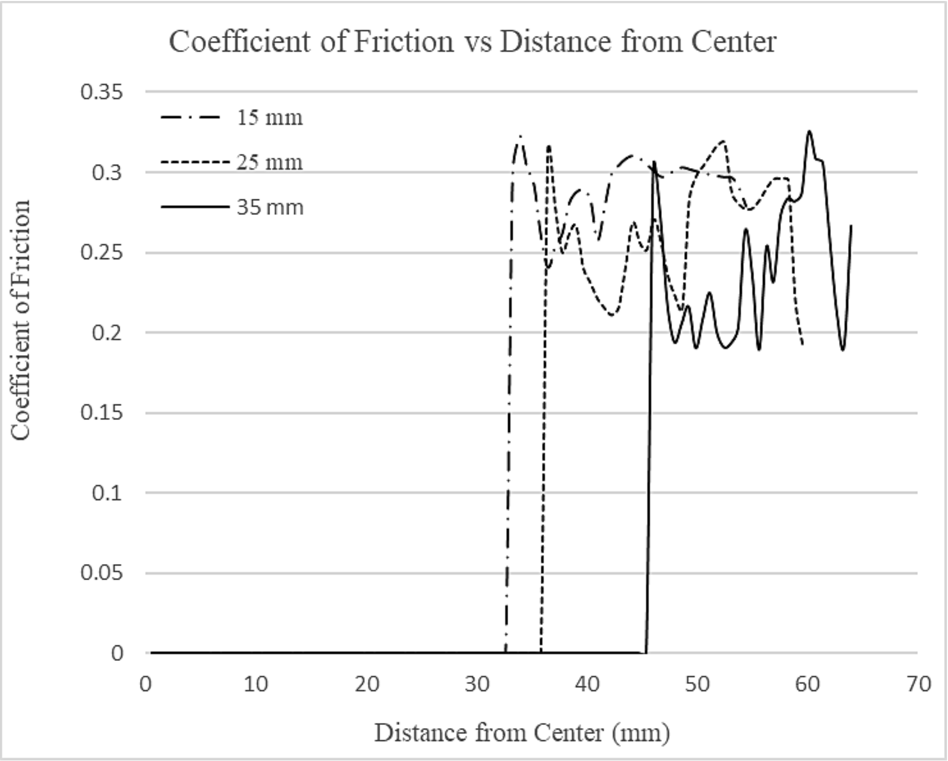

Figure 5.9 Coefficient of friction distribution on 0.64 x 0.64 regions at symmetry plane for 15 mm, 25 mm and 35 mm cup heights (die side)

Since punch is restricted to move with a constant veloctity of 20 mm/s into the drawn part, load on punch changes throughout the simulation. Punch force increases almost linearly up to 20 mm height and reaches 50 kN. Then; punch force rate decreases until the final cup height of 35 mm is reached with 63.1 kN. In order to have a smooth velocity and regular deformation height, control of the punch force is required.

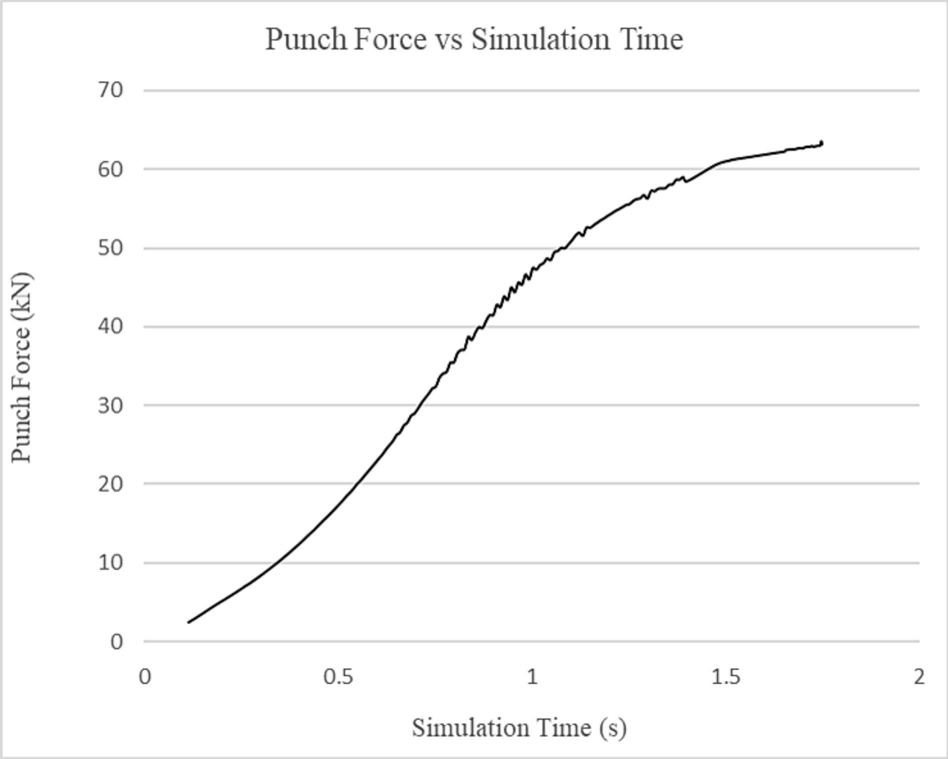

Figure 5.10 Punch force variation over simulation time

Von Mises stress distribution of blank material is shown in Figure 5.11 along the symmetry line for cup heights of 15 mm, 25 mm and 35 mm. Stress varies within a 100 MPa range for 15 mm cup height and increases as the cup height increases. It is seen that the stress under punch nose contact area is small (620-700 MPa) for 25 mm and 35 mm cup heights while highest stresses at the flat region between blank holder and die increases up to 1060 MPa. Trends and characteristics of the stress distribution for 25 mm and 35 mm are very similar with a small shift in radial direction.

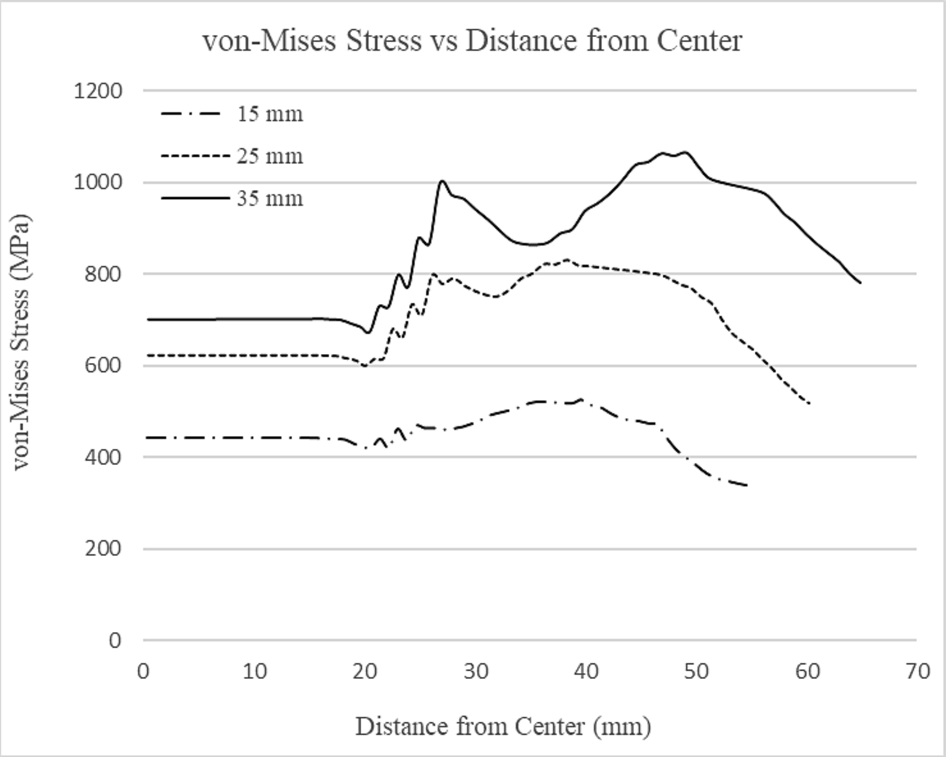

Figure 5.11 Von Mises Stress distribution on nodes at symmetry plane for 15 mm, 25 mm and 35 mm cup heights

Thickness strain distributions for cup heights of 15 mm, 25 mm and 35 mm are shown in Figure 5.12 for drawn steel blank. For all heights, thickness strain is almost constant at the punch nose contact regions and negative which means thinning of the part. Then; at the punch radius contact region there is excessive thinning observed due to deformation of the blank. After punch contact ends, thickness strain reverses trend up to positive values and thickening of the part is observed at the edge of the part. Strain change is almost linear and maximum of 0.082 is reached at cup height of 35 mm.

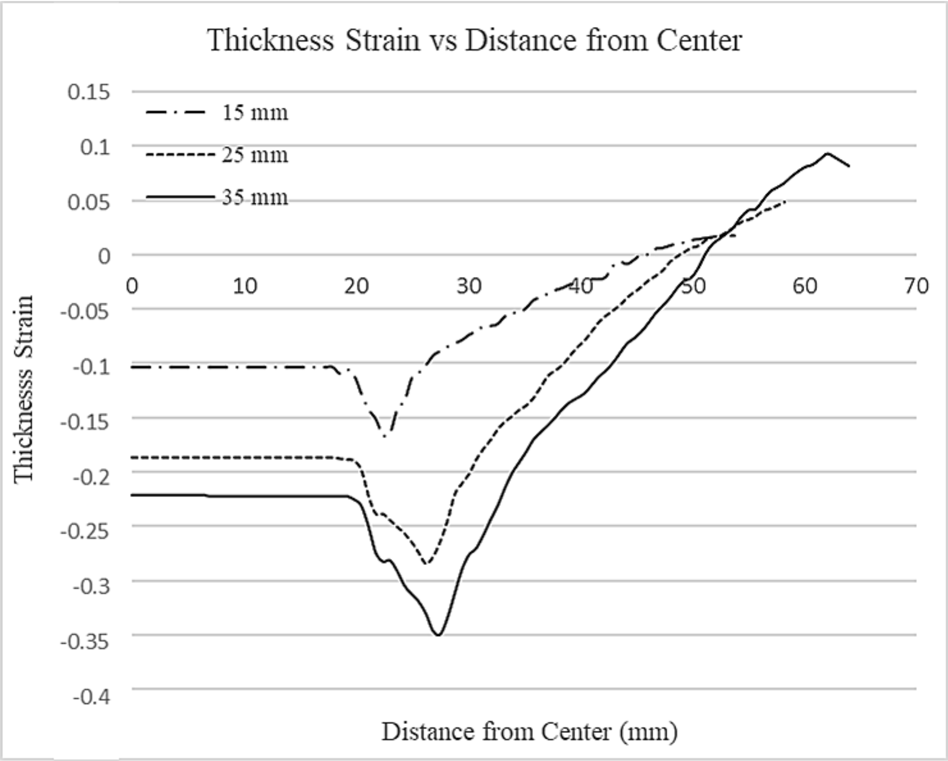

Figure 5.12 Thickness strain distribution on nodes at symmetry plane for 15 mm, 25 mm and 35 mm cup heights

CHAPTER 6

CONCLUSIONS

In this chapter; conclusions of the PhD study are summarized and contributions to the tribology field are emphasized. Then; further work to be followed in next studies are described briefly.

6.1 Conclusions

Simulation of a cylindrical cup drawing is performed using the average coefficients of friction calculated by the proposed friction model. The friction model takes into account the real surface roughnesses, surface simplification with curved surfaces, junction growth, ploughing of the asperities and lubrication. The following are concluded;

1. Measured surface roughness distribution showed that geometry of real surfaces have directional properties. Therefore; surface roughnesses are simplified by using macro asperities defined by curved surfaces having different radiuses of curvature in perpendicular directions.
2. Using curved surfaces gives advantage of dealing with smaller number of macro asperities; 56 macro asperity for an 0.64 mm x 0.64 mm area, which is 3-4 times less than the number of macro asperities that would be necessary if surface had been defined by spherical asperities. Radius of curvatures of macro asperities are observed to vary between 400-1900 μm.
3. The junction growth approximation equations, which are derived in terms of radius of curvature ratio (R_x/R_y), tangential load to normal load ratio (Q/P) and non-dimensional normal load (P^*), are found to be robust and easily applicable with simple and basic parameters.

4. A method is proposed to determine relation between the solid (real) contact area ratio (A_{sol}/A_0) and normal load (P) using the finite element simulation results of measured roughness deformation.
5. An alternative method is proposed for calculation of the shear force due to asperity ploughing of tooling asperities. Previous approaches calculated the shear stress without considering the movement of workpiece with respect to tooling while current simulation method gives better approximation due to consideration of sliding effects and use of different attack angles of 0°, 30°, 60° and 90° with respect to sliding direction.
6. It is found out that, the lubricant property is an important factor on the calculation of shear stress due to indented tooling asperities. Coefficient of friction and consequently the quality of the final drawn part is highly affected by the type of lubricant used.

6.2 Further Work

It is concluded that the coefficient of friction is highly dependent on the lubricant properties as well as surface topography of the blank and tooling. Instead of using a commercial lubricant for reference; properties and boundary shear strength of available lubricants must be calculated with an experimental setup.

All the real measured data used for the deep drawing simulation must be verified with a cup drawing process in an experimental setup for different cup heights. Then; simulation results must be compared with the punch force and strain distribution of the blank.

REFERENCES

[1] Patir N, Cheng HS. Average flow model for determining effects of three dimensional roughness on partial hydrodynamic lubrication. ASME Journal of Lubrication Technology 1978;100(1):12-17.

[2] Patir N, Cheng HS. Application of average flow model to lubrication between rough sliding surfaces. ASME Journal of Lubrication Technology 1979;101(2):220-230.

[3] Shisode M, Hazrati J, Mishra T, de Rooij M, van den Boogard T. Mixed lubrication friction model including surface texture effects for sheet metal forming 2021;291:117035.

[4] Westeneng, J. Modelling of contact and friction in deep drawing processes 2001. University of Twente. PhD Thesis.

[5] Başpınar M. Modelling and Simulation of friction in deep drawing. METU. 2011.

[6] Godfrey, D. Boundary lubrication. P. M. Ku 1968;335-384.

[7] Greenwood JA, Williamson JBP. Contact of nominally flat surfaces. Proc R Soc London 1966;295:300-319.

[8] Greenwood JA, Tripp JH. Contact of two nominally flat rough surfaces. Proc Inst Mech Eng 1970;185:625-633.

[9] Jamari J, Schipper DJ. Plastic deformation and contact area of an elastic–plastic contact of ellipsoid bodies after unloading. Tribology International. 2007(40):1311-1318.

[10] Chung JC. Elastic–plastic contact analysis of an ellipsoid and a rigid flat. Tribology International. 2010(43):491-502.

[11] Horng JH. An elliptic elastic-plastic asperity microcontact model for rough surfaces. Transactions of the ASME. 1998(120):82-88.

[12] Jamari J. An Elliptic Elastic-Plastic Asperity Micro-Contact Model. ROTASI. 2006(8):1-5.

[13] Chung JC. The Elliptical Elastic-Plastic Microcontact Analysis, New Tribological Ways. 2011. ISBN: 978-953-307-206-7.

[14] Catteneo C. Sul Contatto di due Corpi Elastici: Distribuzione Locale Degli Sforzi. Rend. Accad. Naz. Lincei. 1938(27):342-348, 434-436, 474-478.

[15] Mindlin RD. Compliance of Elastic Bodies in Contact. ASME J. Appl. Mech. 1949(16):259-268.

[16] McFarlane JS, Tabor D. “Relation Between Friction and Adhesion”. Proc. R. Soc. London, Ser. A. 1950(202):244-253.

[17] Zolotarevskiy V, Kligerman Y, Etsion I. The Evolution of Static Friction for Elastic-Plastic Spherical Contact in Pre-sliding. 2011(133):034502-1-3.

[18] Kogut L, Etsion I. A Semi-Analytical Solution for the Sliding Inception of a Spherical Contact. Journal of Tribology. 2003(125):499-506.

[19] Brizmer V, Kligerman Y, Etsion I. The effect of contact conditions and material properties on the elasticity terminus of a spherical contact. International Journal of Solids and Structures 2006(43):5736–5749

[20] Brizmer V, Kligerman Y, Etsion I. A model for junction growth of a spherical contact under full stick condition. ASME Journal of Tribology 2007(129):783-790.

[21] Ovcharenko A, Halperin G, Etsion I. In situ and real-time optical investigation of junction growth in spherical elastic–plastic contact. Wear. 2008(264):1043–1050.

[22] Başpınar M, Akkök M. Modeling and Simulation of Friction in Deep Drawing. Journal of Tribology 2015;138(2):021104.

[23] Sojoudi H, Khonsari MM. On the modeling of quasi-steady and unsteady dynamic friction in sliding lubricated line contact. Journal of Tribology 2010;132(1):1-9.

[24] Wilson WRD, Hsu TC, Huang XB. A realistic friction model for computer simulation of sheet metal forming processes. ASME Journal of Engineering for Industry 1995;117:202–9.

[25] Onions RA, Archard JF. The contact of surfaces having a random structure. Journal of Physics D: Applied Physics 1973;6(3):289-304.

[26] Chang WR, Etsion I, Bogy DB. An elastic-plastic model for the contact of rough surfaces. ASME Journal of Tribology 1987;109:257-263.

[27] Halling J, Arnell RD, Nuri KA. The elastic-plastic contact of rough surfaces and its relevance in the study of wear. Proc Inst Mech Eng 1988;202:269-274.

[28] Liu G, Wang Q, Lin C. A survey of current models for simulating the contact between rough surfaces. Tribology Transactions 1999;42(3):581-591.

[29] Webster MN, Sayles RS. Numerical model for the elastic frictionless contact of real rough surfaces. Journal of Tribology 1986;108(3):314-320.

[30] Sutcliffe MPF. Surface asperity deformation in metal forming processes. International Journal of Mechanical Sciences 1988;30(11):847-868.

[31] Wilson WRD, Sheu S. Real area of contact and boundary friction in metal forming. International Journal of Mechanical Sciences 1988;30(7):475-489.

[32] Kimura Y, Childs THC. Surface asperity deformation under bulk plastic straining conditions. International Journal of Mechanical Sciences 1999;41(3):283-307.

[33] Pullen J, Williamson JPB. On the plastic contact of rough surfaces. Proc. R. Soc. London, Series A 1972;327:159-173.

[34] Vyas P. Effects of stochastic (random) surface roughnesson hydrodynamic lubrication of deterministic asperity 2005. University of Kentucky. Master’s Thesis.

[35] Sinkhonde D. A contribution to debate on surface roughness of clay brick powder generated using varying milling treatments. Results in Engineering. 2023(19):101236.

[36] Dizeci Ş. An investigation of ductile fracture criteria for sheet metal forming 2014. METU. PhD Thesis.

[37] Kogut L, Etsion I. Elastic-Plastic Contact Analysis of a Sphere and a Rigid Flat. ASME Journal of Applied Mechanics. 2002;69:657-662.

[38] Brizmer V, Kligerman Y, Etsion I. The effect of contact conditions and material properties on the elasticity terminus of a spherical contact. International Journal of Solids and Structures 2006;43:5736–5749

[39] Hol J, Meinders V, Geijselaers H, van den Boogaard A. Multi-scale friction modeling for sheet metal forming: the mixed lubrication regime. Tribol. Int. 2015a;85:10–25.

[40] Hol J, Meinders V, de Rooij M, van den Boogaard A. Multi-scale friction modeling for sheet metal forming: the boundary lubrication regime. Tribol. Int. 2015b;81:112–128.

[41] Shisode M, Hazrati J, Mishra T, de Rooij M, van den Boogaard A. Semianalytical contact model to determine the flattening behavior of coated sheets under normal load. Tribol. Int. 202a;106182.

[42] Shisode M, Hazrati J, Mishra T , de Rooij M, ten Horn C, van Beeck J, van den Boogaard A. Modeling boundary friction of coated sheets in sheet metal forming applications. Tribol. Int. 2020b;106554.

[43] Mishra T, de Rooij MB, Shisode M, Hazrati J, Schipper DJ. Characterization of interfacial shear strength and its effect on ploughing behaviour in single-asperity sliding. Wear 2019;436:203042.

[44] Pan P, Hamrock BJ. Simple Formulae for performance of parameters used in

elastohydrodynamically lubricated line contacts. ASME Journal of Tribology 1989;112(2):26-304.

APPENDICES

A. Junction growth equation of an elliptical body with radius of curvature ratio of 0.6

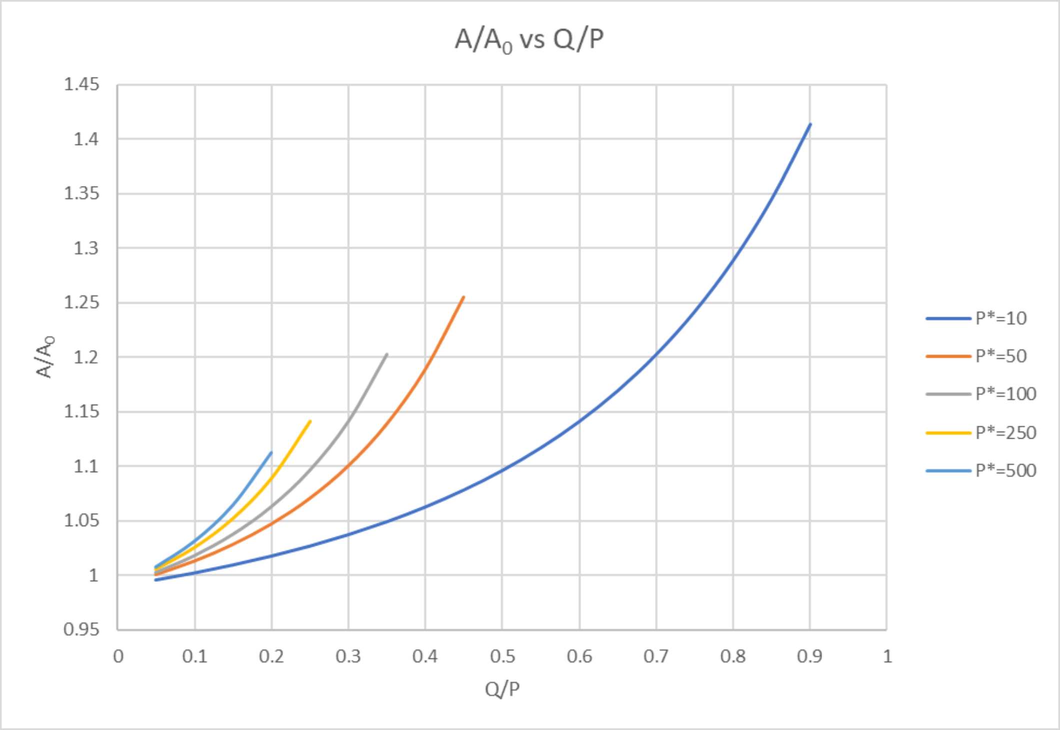

B. Junction growth equation of an elliptical body with radius of curvature ratio of 0.5

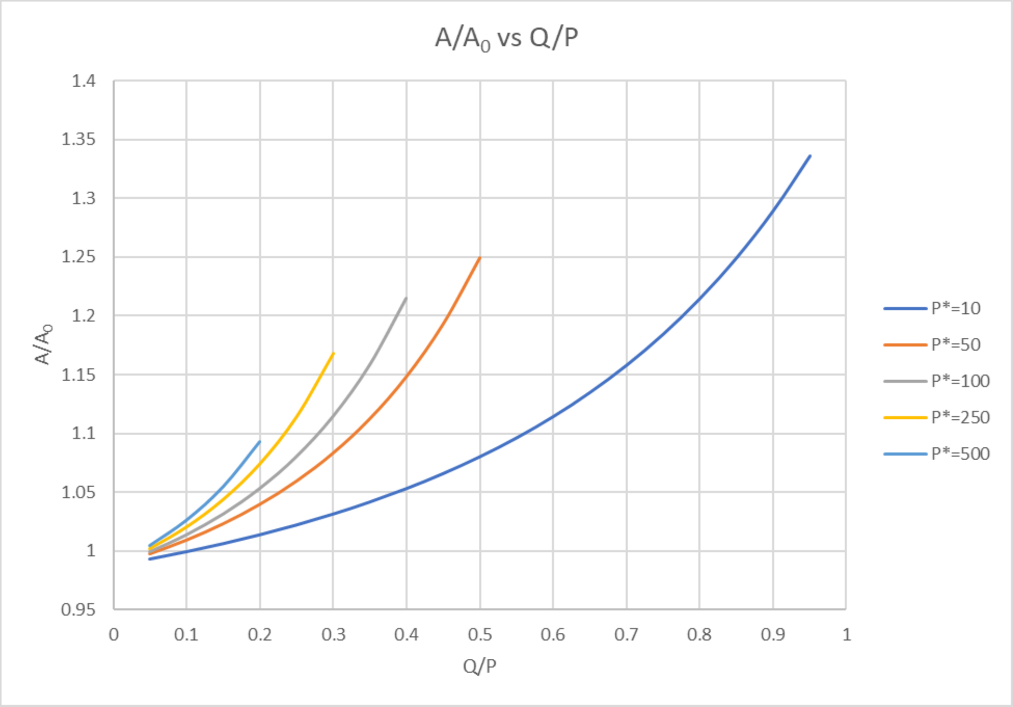

CURRICULUM VITAE

Surname, Name: Başpınar, Murat

EDUCATION

Degree	**Institution**	**Year of Graduation**
MS	METU Mechanical Engineering	2011
BS	METU Mechanical Engineering	2008
High School	Kocaeli Anadolu High School, Ankara	2004

FOREIGN LANGUAGES

Advanced English

PUBLICATIONS

1. Başpınar M, Akkök M. Modeling and Simulation of Friction in Deep Drawing. Journal of Tribology 2015;138(2):021104.